

# Mesons as Bound States of Confined Quarks: Zero and Finite Temperature

Pieter Maris\* and Peter C. Tandy

*Center for Nuclear Research, Department of Physics,  
Kent State University, Kent OH 44242, USA.*

**ABSTRACT:** We survey recent work on the properties and decays of mesons as bound states of confined quarks at both zero and finite temperature. The framework for these investigations is the set of QCD Dyson–Schwinger equations truncated to ladder-rainbow level. The infrared structure of the ladder-rainbow kernel is described by two parameters; the ultraviolet behavior is fixed by the one-loop renormalization group behavior of QCD. The work is restricted to the  $u$ ,  $d$  and  $s$  quark sector and allows a Poincaré-covariant study of the masses and electroweak decay constants of the ground state pseudoscalars and vectors:  $\pi$ ,  $K$ ,  $\rho/\omega$ ,  $K^*$  and  $\phi$ . Within the impulse approximation, we summarize results for the  $\pi$  and  $K$  charge form factors. Their timelike behavior exhibits the vector meson production resonances and from this the associated vector meson strong decay constants are extracted. The confining property of the quark self-energy dynamically produced in this work prevents the appearance of spurious  $\bar{q}q$  production effects. The finite temperature behavior of this model, and closely related ones, is summarized for: the chiral restoration transition, the deconfinement transition, the  $T$ -dependence of the spatial meson mode masses, and the  $T$ -dependence of selected electroweak and strong decay widths. The  $T$ -dependence obtained for meson masses is compared to results from lattice QCD.

**KEYWORDS:** Dyson–Schwinger Equations, Bethe–Salpeter Equation, Meson Masses, Decays and Form Factors, Confinement, Dynamical Chiral Symmetry Breaking, Finite Temperature QCD, Chiral Restoration Transition,  $T$ -dependence of Meson Properties.

## 1. Introduction

The light pseudoscalar mesons play an important role in understanding low-energy QCD. They are the lightest observable hadronic bound states of a quark and an antiquark, and are the Goldstone bosons associated with chiral symmetry breaking. Their static properties such as the mass and decay constants have been studied extensively and are qualitatively understood within QCD. A number of studies of pseudoscalar mesons [1–3] have played a key role in the development of continuum methods for modeling QCD via the Dyson–Schwinger equations [DSEs]. Such methods have now evolved

into an excellent tool for the study of nonperturbative aspects of a variety hadronic properties and processes in QCD [4–6].

Here we recall recent studies of light mesons, both at zero temperature and at finite temperature, in which the quark propagator DSE in the  $u$ ,  $d$  and  $s$  quark sector is coupled to the meson bound state Bethe–Salpeter equation [BSE]. The bound state amplitudes so produced are used to study meson decays and form factors. This approach is consistent with quark and gluon confinement [5–7], generates dynamical chiral symmetry breaking [8], and is explicitly Poincaré covariant. It is straightforward to implement the correct one-loop renormalization group behavior of QCD [3],

\*Present address: Dept. of Physics, North Carolina State University, Raleigh, NC 27695-8202, USA.

and to obtain agreement with perturbation theory in the perturbative region. Provided that the relevant Ward–Takahashi identities [WTI] are preserved in the truncation of the DSEs, the corresponding currents are conserved. The axial WTI ensures the Goldstone nature of the pions [9]; the vector WTI is important for electromagnetic current conservation.

We show results for the pion and kaon electromagnetic form factors in impulse approximation [10,11], both in the timelike and the space-like region. In impulse approximation, with quark propagators dressed in rainbow approximation and meson Bethe–Salpeter amplitudes produced in ladder approximation, the vector WTI for the quark-photon vertex ensures that the meson electromagnetic current is conserved. A feature of this work is that the confining property of the dynamically generated quark self-energy prevents the appearance of spurious  $\bar{q}q$  production effects in the timelike region. The ground state vector mesons provide the lowest physical resonances in the structure of the timelike charge form factors of the pion and kaon. We summarize the ladder-rainbow DSE-BSE results for the ground state vector mesons [12] as well as their strong and electroweak decays. The various strong and electromagnetic interactions involving vector and pseudoscalar mesons have been a typical testing ground for non-perturbative QCD models [4] and here we give a few examples of modern treatments of such processes.

At finite temperature we discuss chiral restoration and deconfinement using the Matsubara formalism. In rainbow-ladder truncation, there is a second-order, mean field chiral phase transition, with a critical temperature around 120 ~ 150 MeV depending on the details of the ladder kernel [13]. We also summarize results for the temperature dependence of the spatial masses of the scalar, pseudoscalar, and vector  $\bar{q}q$  bound states and selected electroweak and strong decay widths of these spatial  $\bar{q}q$  modes [14,15]. Despite deconfinement, these modes seem to persist above the chiral and deconfinement phase transition. The results for the  $T$ -dependence of spatial meson masses

are in reasonable qualitative agreement with results from lattice QCD.

In the next Section we give the relevant DSEs, followed by a discussion of the truncation and the model parameters in Sec. 3. In Sec. 4 we discuss in detail the application of the DSE approach to calculate meson electromagnetic form factors. Modifications of the model to study QCD at finite temperature are considered in Sec. 5 and there we also discuss the chiral phase transition. Sec. 6 covers the temperature dependence of properties of spatial  $\bar{q}q$  modes, including masses and decays. Finally we conclude in Sec. 7.

## 2. Dyson–Schwinger equations

The dressed quark propagator  $S(q)$  is the solution of the DSE<sup>1</sup>

$$S(p)^{-1} = Z_2 i \not{p} + Z_4 m(\mu) + Z_1 \int_q^\Lambda g^2 D_{\mu\nu}(k) \frac{\lambda^i}{2} \gamma_\mu S(q) \Gamma_\nu^i(q, p), \quad (2.1)$$

where  $D_{\mu\nu}(k = p - q)$  is the renormalized dressed-gluon propagator, and  $\Gamma_\nu^i(q, p)$  is the renormalized dressed quark-gluon vertex. The notation  $\int_q^\Lambda \equiv \int^\Lambda d^4q / (2\pi)^4$  stands for a translationally invariant regularization of the integral, with  $\Lambda$  being the regularization mass-scale. The regularization can be removed at the end of all calculations, and after renormalization, by taking the limit  $\Lambda \rightarrow \infty$ . The solution of Eq. (2.1) is renormalized according to  $S(p)^{-1} = i \not{p} + m(\mu)$  at a sufficiently large spacelike  $\mu^2$ , with  $m(\mu)$  the renormalized quark mass at the scale  $\mu$ . In Eq. (2.1),  $S$ ,  $\Gamma_\mu^i$  and  $m(\mu)$  depend on the quark flavor, although we have not indicated this explicitly. The renormalization constants  $Z_2$  and  $Z_4$  depend on the renormalization point and the regularization mass-scale, but not on flavor: in our analysis we employ a flavor-independent renormalization scheme.

The Bethe–Salpeter amplitude [BSA] for a meson bound state of a quark  $a$  having momentum  $q_+$  and an antiquark  $b$  having momentum  $q_-$

<sup>1</sup>We use Euclidean metric  $\{\gamma_\mu, \gamma_\nu\} = 2\delta_{\mu\nu}$ ,  $\gamma_\mu^\dagger = \gamma_\mu$  and  $a \cdot b = \sum_{i=1}^4 a_i b_i$ .

is denoted by  $\Gamma^{a\bar{b}}(q_+, q_-)$ . The meson momentum is  $P = q_+ - q_-$  and satisfies  $P^2 = -m^2$ . The BSAs are solutions of the homogeneous BSE

$$\Gamma^{a\bar{b}}(p_+, p_-) = \int_q^\Lambda K(p, q; P) \chi^{a\bar{b}}(q_+, q_-), \quad (2.2)$$

which has solutions at discrete values of  $P^2$  only. Here,  $K$  is the renormalized  $\bar{q}q$  scattering kernel that is irreducible with respect to a pair of  $\bar{q}q$  lines, and  $\chi^{a\bar{b}}(q, q') = S^a(q)\Gamma^{a\bar{b}}(q, q')S^{\bar{b}}(q')$  is the Bethe-Salpeter wavefunction. In order to implement Eq. (2.2) while preserving the constraint  $P = q_+ - q_-$ , it is necessary to specify how the total momentum is partitioned between the quark and the antiquark. The general choice is  $q_+ = q + \eta P$  and  $q_- = q - (1 - \eta)P$  where  $\eta$  is the momentum partitioning parameter. The choice of  $\eta$  corresponds to the choice of relative momentum; physical observables should not depend on the choice. This provides us with a convenient check on the accuracy of the numerics in an actual model calculation.

The meson BSA  $\Gamma^{a\bar{b}}$  is normalized according to the canonical normalization condition

$$2P_\mu = N_c \frac{\partial}{\partial P_\mu} \left\{ \int_q^\Lambda \text{tr}_s [\bar{\Gamma}^{a\bar{b}}(\tilde{q}', \tilde{q}) S^a(q_+) \Gamma^{a\bar{b}}(\tilde{q}, \tilde{q}') S^{\bar{b}}(q_-)] + \int_{k,q}^\Lambda \text{tr}_s [\bar{\chi}^{a\bar{b}}(\tilde{k}', \tilde{k}) K(k, q; P) \chi^{a\bar{b}}(\tilde{q}, \tilde{q}')] \right\}, \quad (2.3)$$

at the meson mass shell  $P^2 = Q^2 = -m^2$ , with  $\tilde{q} = q + \eta Q$ ,  $\tilde{q}' = q - (1 - \eta)Q$ , and similarly for  $\tilde{k}$  and  $\tilde{k}'$ . The notation  $\text{tr}_s$  denotes a trace over Dirac spin. For the antimeson BSA we have used the notation  $\bar{\Gamma}(q_-, q_+) = [C^{-1}\Gamma(-q_+, -q_-)C]^t$  in which  $C = \gamma_2\gamma_4$  is the charge conjugation matrix, and  $X^t$  denotes the matrix transpose of  $X$ .

For pseudoscalar bound states the BSA is commonly decomposed into [3]

$$\Gamma(k + \eta P, k - (1 - \eta)P) = \gamma_5 [iE + \not{P}F + \not{k}G + \sigma_{\mu\nu} k_\mu P_\nu H], \quad (2.4)$$

where the invariant amplitudes  $E$ ,  $F$ ,  $G$  and  $H$  are Lorentz scalar functions  $f(k^2, k \cdot P; \eta)$ . The dependence of the amplitudes upon  $k \cdot P$  can be conveniently represented by the following expansion based on Chebyshev polynomials

$$f(k^2, k \cdot P) = \sum_{i=0}^{\infty} U_i(\cos \theta) (kP)^i f_i(k^2), \quad (2.5)$$

where  $\cos \theta = k \cdot P / (kP)$ . For charge-parity eigenstates such as the pion, each amplitude  $E$ ,  $F$ ,  $G$ , and  $H$  will have a well-defined parity in the variable  $k \cdot P$  if one chooses  $\eta = \frac{1}{2}$ . In this case, these amplitudes are either entirely even ( $E$ ,  $F$ , and  $H$ ) or odd ( $G$ ) in  $k \cdot P$ , and only the even ( $E$ ,  $F$ , and  $H$ ) or odd ( $G$ ) Chebyshev moments  $f_i$  are needed for a complete description.

### 3. Ladder-rainbow model

We employ a model that has been developed recently for an efficient description of the masses and decay constants of the light pseudoscalar and vector mesons [3,12]. This consists of the rainbow truncation of the DSE for the quark propagator and the ladder truncation of the BSE for the meson BSAs. The required effective  $\bar{q}q$  interaction is constrained by perturbative QCD in the ultraviolet and has a phenomenological infrared behavior. In particular, the rainbow truncation of the quark DSE, Eq. (2.1), is

$$Z_1 g^2 D_{\mu\nu}(k) \Gamma_\nu^i(q, p) \rightarrow \mathcal{G}(k^2) D_{\mu\nu}^{\text{free}}(k) \gamma_\nu \frac{\lambda^i}{2}, \quad (3.1)$$

where  $D_{\mu\nu}^{\text{free}}(k = p - q)$  is the free gluon propagator in Landau gauge. The consistent ladder truncation of the BSE, Eq. (2.2), is

$$K(p, q; P) \rightarrow -\mathcal{G}(k^2) D_{\mu\nu}^{\text{free}}(k) \frac{\lambda^i}{2} \gamma_\mu \otimes \frac{\lambda^i}{2} \gamma_\nu, \quad (3.2)$$

where  $k = p - q$ . These two truncations are consistent in the sense that the combination produces vector and axial-vector vertices satisfying the respective WTI. In the axial case, this ensures that in the chiral limit the ground state pseudoscalar mesons are the massless Goldstone bosons associated with chiral symmetry breaking; with nonzero

current quark masses it leads to a generalisation of the Gell-Man–Oaks–Renner relation [9]. In the vector case, this ensures conservation of the meson electromagnetic current in impulse approximation as described in the next section.

The model is completely specified once a form is chosen for the “effective coupling”  $\mathcal{G}(k^2)$ . The ultraviolet behavior is chosen to be that of the QCD running coupling  $\alpha(k^2)$ ; the ladder-rainbow truncation then generates the correct perturbative QCD structure of the DSE-BSE system of equations. The phenomenological infrared form of  $\mathcal{G}(k^2)$  is chosen so that the DSE kernel contains sufficient infrared enhancement to produce an empirically acceptable amount of dynamical chiral symmetry breaking as represented by the chiral condensate [16].

We employ the Ansatz found to be successful for the light mesons in Refs. [3,12]

$$\frac{\mathcal{G}(k^2)}{k^2} = \frac{4\pi^2 D k^2}{\omega^6} e^{-k^2/\omega^2} + \frac{4\pi^2 \gamma_m \mathcal{F}(k^2)}{\frac{1}{2} \ln \left[ \tau + \left( 1 + k^2/\Lambda_{\text{QCD}}^2 \right)^2 \right]}, \quad (3.3)$$

with  $\gamma_m = \frac{12}{33-2N_f}$  and  $\mathcal{F}(s) = (1 - \exp(\frac{-s}{4m_t^2}))/s$ . The first term implements the strong infrared enhancement in the region  $0 < k^2 < 1 \text{ GeV}^2$  required for sufficient dynamical chiral symmetry breaking. The second term serves to preserve the one-loop renormalization group behavior of QCD. We use  $m_t = 0.5 \text{ GeV}$ ,  $\tau = e^2 - 1$ ,  $N_f = 4$ , and we take  $\Lambda_{\text{QCD}} = 0.234 \text{ GeV}$ . The renormalization scale is chosen to be  $\mu = 19 \text{ GeV}$  which is well into the domain where one-loop perturbative behavior is appropriate [3,12]. The remaining parameters,  $\omega = 0.4 \text{ GeV}$  and  $D = 0.93 \text{ GeV}^2$  along with the quark masses, are fitted to give a good description of  $\langle \bar{q}q \rangle$ ,  $m_{\pi/K}$  and  $f_\pi$ . The subsequent values for  $f_K$  and the masses and decay constants of the vector mesons  $\rho, \phi, K^*$  are found to be within 10% of the experimental data [12], see Table 1. A detailed analysis of the relationship between QCD and this Landau gauge, rainbow-ladder truncation of the DSEs with renormalization group improvement, can be found in the originating work [3]. A com-

	experiment (estimates)	calculated ( <sup>†</sup> fitted)
$m_{\mu=1\text{GeV}}^{u=d}$	5 - 10 MeV	5.5 MeV
$m_{\mu=1\text{GeV}}^s$	100 - 300 MeV	125 MeV
$-\langle \bar{q}q \rangle_\mu^0$	$(0.236 \text{ GeV})^3$	$(0.241^\dagger)^3$
$m_\pi$	0.1385 GeV	0.138 <sup>†</sup>
$f_\pi$	0.131 GeV	0.131 <sup>†</sup>
$m_K$	0.496 GeV	0.497 <sup>†</sup>
$f_K$	0.160 GeV	0.155
$m_\rho$	0.770 GeV	0.742
$f_\rho$	0.216 GeV	0.207
$m_{K^*}$	0.892 GeV	0.936
$f_{K^*}$	0.225 GeV	0.241
$m_\phi$	1.020 GeV	1.072
$f_\phi$	0.236 GeV	0.259

**Table 1:** Overview of the results of the model for the meson masses and decay constant, adapted from Ref. [12]. The experimental value for the condensate is taken from Ref. [20], the other experimental data are from Ref. [21].

parison with lattice QCD results [17] confirms the qualitative behavior for the dressed quark propagator produced by this model [18,19].

Recent reviews [5,6,22] put this model in a wider perspective. These reviews include a compilation of results for both meson and baryon physics with similar models, an analysis of how quark confinement is manifest in solutions of the DSEs, and both finite temperature and finite density extensions. The question of the accuracy of the ladder-rainbow truncation has also received some attention; it was found to be particularly suitable for the flavor octet pseudoscalar mesons and for the vector mesons, since the next-order contributions in a quark-gluon skeleton graph expansion have a significant amount of cancellation between repulsive and attractive corrections [23].

#### 4. Electromagnetic form factors in impulse approximation

The 3-point function describing the coupling of a photon with momentum  $Q$  to a pseudoscalar meson, with initial and final momenta  $P \pm Q/2$ , can

be written as the sum of two terms

$$\Lambda_\nu^{a\bar{b}}(P, Q) = \hat{Q}^a \Lambda_\nu^{a\bar{b}a} + \hat{Q}^{\bar{b}} \Lambda_\nu^{a\bar{b}b}, \quad (4.1)$$

where  $\hat{Q}$  is the quark or antiquark electric charge, and where  $\Lambda^{a\bar{b}a}(P, Q)$  and  $\Lambda^{a\bar{b}b}(P, Q)$  describe the coupling of a photon to the quark ( $a$ ) and anti-quark ( $\bar{b}$ ) respectively. The meson form factor is defined by

$$\Lambda_\nu^{a\bar{b}}(P, Q) = 2 P_\nu F(Q^2), \quad (4.2)$$

with the charge radius defined by  $r^2 = -6F'(0)$ . Analogously, we can define a form factor for each of the two terms on the RHS of Eq. (4.1), for example

$$\Lambda_\nu^{a\bar{b}b}(P, Q) = 2 P_\nu F_{a\bar{b}b}(Q^2). \quad (4.3)$$

Current conservation dictates that each of the form factors  $F_{a\bar{b}b}(Q^2)$  and  $F_{a\bar{b}a}(Q^2)$  is one at  $Q^2 = 0$ .

The impulse approximation allows form factors to be described in terms of dressed quark propagators, bound state BSAs, and the dressed  $q\bar{q}\gamma$ -vertex. We denote by  $\Gamma_\mu^a(q_+, q_-)$  the vertex describing the coupling of a photon with momentum  $Q = q_+ - q_-$  to a quark of flavor  $a$  with final and initial momenta  $q_+$  and  $q_-$  respectively. With this notation, the vertices in Eq. (4.1) take the form [11]

$$\begin{aligned} \Lambda_\nu^{a\bar{b}b}(P, Q) = N_c \int_k^\Lambda \text{tr}_s [S^a(q) \Gamma^{a\bar{b}}(q, q_+) S^b(q_+) \\ \times i\Gamma_\nu^b(q_+, q_-) S^b(q_-) \bar{\Gamma}^{a\bar{b}}(q_-, q)], \end{aligned} \quad (4.4)$$

where  $q = k + P/2$  and  $q_\pm = k - P/2 \pm Q/2$ . The expression for  $\Lambda_\nu^{a\bar{b}a}$  is analogous.

#### 4.1 The quark-photon vertex

The quark-photon vertex is the solution of the renormalized inhomogeneous BSE with the same kernel  $K$  as the homogeneous BSE for meson bound states. That is, for photon momentum  $Q$ ,

$$\begin{aligned} \Gamma_\mu^a(p_+, p_-) = Z_2 \gamma_\mu + \int_q^\Lambda K(p, q; Q) S^a(q_+) \\ \times \Gamma_\mu^a(q_+, q_-) S^a(q_-), \end{aligned} \quad (4.5)$$

with  $p_\pm = p \pm Q/2$  and  $q_\pm = q \pm Q/2$ . Because of gauge invariance, it satisfies the WTI

$$i Q_\mu \Gamma_\mu^a(p_+, p_-) = S_a^{-1}(p_+) - S_a^{-1}(p_-). \quad (4.6)$$

The general form of the quark-photon vertex  $\Gamma_\mu^a(q; Q)$  requires a decomposition into twelve independent Lorentz covariants, which can be made from the three vectors  $\gamma_\mu$ , the relative momentum  $q_\mu$ , and the photon momentum  $Q_\mu$ , each multiplied by one of the four independent matrices  $\mathbf{1}$ ,  $\not{q}$ ,  $\not{Q}$ , and  $\sigma_{\mu\nu} q_\mu Q_\nu$ . Four of the covariants represent the longitudinal components which are completely specified by the WTI in terms of the quark propagator and they do not contribute to elastic form factors. The solution of the BSE for the transverse vertex can be expanded in eight covariants  $T_\mu^i(q; Q)$  with the corresponding amplitudes being Lorentz scalar functions. The choice of covariant basis  $T_\mu^i(q; Q)$  is constrained by the required properties under Lorentz and CPT transformations, but is not unique. A convenient basis that facilitates projection of the BSE, Eq. (4.5), has been given in Ref. [10] and a discussion of the results for the vertex can also be found there.

Note that solutions of the homogeneous version of Eq. (4.5) define vector meson bound states with masses  $m_V^2 = -Q^2$  at discrete timelike momenta  $Q^2$ . It follows that  $\Gamma_\mu^a$  has poles at those locations and, in the vicinity of the bound states, behaves like [10]

$$\Gamma_\mu^a(p_+, p_-) \rightarrow \frac{\Gamma_\mu^{a\bar{a}V}(p_+, p_-) f_V m_V}{Q^2 + m_V^2}, \quad (4.7)$$

where  $\Gamma_\mu^{a\bar{a}V}$  is the  $a\bar{a}$  vector meson BSA, and  $f_V$  is the electroweak decay constant. For the photon coupled to  $u$ - and  $d$ -quarks, this results in a  $\rho$ -meson pole at  $Q^2 = -0.6 \text{ GeV}^2$ . We will come back to this behavior in the timelike region in Sec. 4.5.

#### 4.2 Current conservation

At  $Q = 0$  the quark-photon vertex is completely specified by the differential Ward identity

$$i \Gamma_\mu^b(p, p) = \frac{\partial}{\partial p_\mu} S_b^{-1}(p). \quad (4.8)$$

If this is inserted in Eq. (4.4), one finds after a change of integration variables  $k \rightarrow q - P/2$

$$\Lambda_\nu^{a\bar{b}\bar{b}}(P, 0) = 2 P_\mu F_{a\bar{b}\bar{b}}(0) = N_c \int_q^\Lambda \text{tr}_s \left[ \bar{\Gamma}^{a\bar{b}}(q', q) S^a(q) \Gamma^{a\bar{b}}(q, q') \frac{\partial S^b(q')}{\partial P_\mu} \right], \quad (4.9)$$

with  $q' = q - P$ . Comparing this expression to Eq. (2.3) with  $\eta = 0$ , we recognize that the physical result  $F(Q^2 = 0) = 1$  follows directly from the canonical normalization condition for  $\Gamma^{a\bar{b}}$  if the BSE kernel  $K$  is independent of the meson momentum  $P$  and the quark-photon vertex satisfies the differential Ward identity [24].

With an arbitrary value for the momentum partitioning parameter  $\eta$ , the relation between the normalization condition for  $\Gamma^{a\bar{b}}$  and electromagnetic current conservation is not so straightforward. A shift in the value of  $\eta$  in loop diagrams (without external quark lines) is equivalent to a shift in integration variables. For processes that are not anomalous, loop integrals are independent of a shift in integration variables provided that all approximated quantities in the integrand respect Poincaré covariance. In this respect, particular attention must be paid to the representation and approximation used for the BSAs. The general BSE vertex solution  $\Gamma(q_+, q_-)$ , considered as a function of the incoming and outgoing quark momenta, does not depend on  $\eta$ . It is only in commonly used decompositions such as Eq. (2.4), that the value of  $\eta$  becomes relevant. The amplitudes  $E$ ,  $F$ ,  $G$ , and  $H$  are scalar functions of  $k^2$  and  $k \cdot P$  which *do* depend on  $\eta$ , i.e., on the choice of a relative momentum. Under a change of  $\eta$ , some of the different Dirac covariants and associated amplitudes (such as  $F$  and  $G$ ) will mix, as will the various Chebyshev moments  $f_i$  in Eq. (2.5). However, the net result from use of a complete representation of both the Dirac matrix structure and the  $k \cdot P$  variable is independent of  $\eta$  and choice of integration variables in loop integrals; this has been checked explicitly for the decay constants [3] and for form factors [11].

The ladder BSE kernel is independent of the

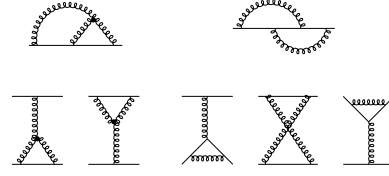


**Figure 1:** The two leading-order vertex corrections to the rainbow DSE (top) and the corresponding five diagrams to be added to the ladder BSE kernel (bottom) for consistency with the relevant WTIs. The quark and gluon lines indicate dressed propagators in this and the subsequent figures.

meson momentum  $P$ , and with quark propagators dressed in rainbow approximation and the dressed quark-photon vertex produced in ladder approximation, the WTI is satisfied [10]; thus impulse approximation for the charge form factor in combination with rainbow-ladder truncation is ideal in the sense that the resulting meson electromagnetic current is conserved. That is, the correct electric charge of the meson is produced independent of the model parameters, and independent of the momentum partitioning parameter  $\eta$ .

### 4.3 Beyond rainbow-ladder truncation

If one goes beyond the rainbow-ladder truncation for the DSEs for the propagators, BSAs and quark-photon vertex, one has to go beyond impulse approximation for the form factors to ensure current conservation [11]. For example, one could include corrections to the rainbow-ladder DSE and BSE kernels that are higher-order in  $\alpha_s$ , as depicted in Fig. 1. Following the general procedure developed in Ref. [23], one can show that both the WTI, Eq. (4.6), and the differential Ward identity, Eq. (4.8), are preserved in the truncation indicated in Fig. 1. Also preserved is the axial-vector WTI, which is important for the Goldstone nature of the pions [9].

The resulting BSE kernel  $K(q, p; P)$  now becomes dependent on the meson momentum  $P$ , which means that the second term of the normalization condition, Eq.(2.3), is nonzero. To be specific, with the choice  $\eta = 0$ , this introduces the

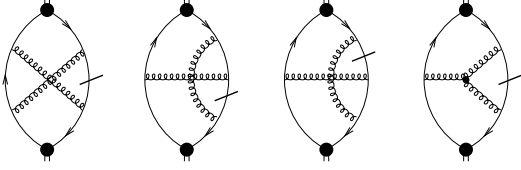


**Figure 2:** The four diagrams arising from the  $P$ -dependence of the kernel in the normalization condition, Eq. (2.3), if one includes the diagrams of Fig. 1 into the DSE dynamics, and chooses all of the meson momentum  $P$  to flow through one quark only. The derivatives with respect to  $P$  are marked by slashes.

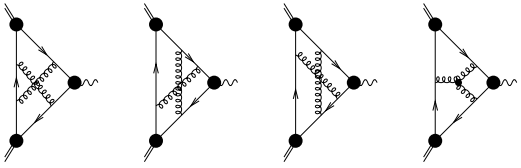


**Figure 3:** The four corrections to the impulse approximation, Eq. (4.4), necessary to maintain current conservation if one includes the diagrams of Fig. 1 into the DSE dynamics.

four extra terms in the normalization condition depicted in Fig. 2. These four additional diagrams are generated from the BSE kernel in the bottom part of Fig. 1 by taking the derivative with respect to the meson momentum  $P$ , where  $P$  flows through one quark propagator only. Since a derivative with respect to  $P$  is equivalent to the insertion of a zero-momentum photon according to the differential WTI, Eq. (4.6), it is obvious which diagrams have to be added to the impulse approximation for the vertex  $\Lambda^{ab\bar{b}}$  to maintain current conservation [11], and they are displayed in Fig. 3. In the limit  $Q \rightarrow 0$  these four additional diagrams become identical to the four additional diagrams in Fig. 2, provided that the vertex satisfies the differential WTI. Of course, there are similar contributions to  $\Lambda^{a\bar{b}a}$ , which can be identified with terms in the normalization condition with  $\eta = 1$ .

A related topic is the correction to the impulse approximation from pion and kaon loops. Simple addition of such loops without supplementing the ladder-rainbow truncation for the DSEs, will gen-

erally violate current conservation. A consistent treatment of the kernels for both the DSE and BSE equations and the approximation for the photon-hadron coupling is necessary for current conservation. At present it is not clear how to incorporate meson loops self-consistently in such an approach, but we expect corrections coming from such loops to be small in the spacelike region. In Ref. [25] it was demonstrated that the dressed quark core can generate most of the pion charge radius, and that pion loops contribute less than 15% to  $r_\pi^2$ . For larger values of  $Q^2$  the effect from meson loops reduces even further, and for  $Q^2 > 1 \text{ GeV}^2$  we expect the contribution of such loops to be negligible.

#### 4.4 Results for the $\pi$ and $K^{0,\pm}$ form factors

The pion and kaon form factors are given by

$$F_\pi(Q^2) = \frac{2}{3}F_{u\bar{d}u}(Q^2) + \frac{1}{3}F_{u\bar{d}\bar{d}}(Q^2), \quad (4.10)$$

$$F_{K^+}(Q^2) = \frac{2}{3}F_{u\bar{s}u}(Q^2) + \frac{1}{3}F_{u\bar{s}\bar{s}}(Q^2), \quad (4.11)$$

$$F_{K^0}(Q^2) = -\frac{1}{3}F_{d\bar{s}d}(Q^2) + \frac{1}{3}F_{d\bar{s}\bar{s}}(Q^2), \quad (4.12)$$

where the quark and antiquark charges are evident. It is only recently that a consistent implementation of the impulse approximation for these form factors has been carried out with solutions of the ladder-rainbow DSEs for each required element: propagators, meson BSAs, and the photon-quark vertex [11,10]. Non-analytic effects from vector mesons are automatically taken into account, because these vector  $\bar{q}q$  bound states appear as poles in the quark-photon vertex solution [10].

We employ the model described in Sec. 3, without any parameter adjustment. Since we work in the SU(2) isospin limit,  $u$  and  $d$  quarks are identical apart from their charge, and we have for the pion electromagnetic form factor simply  $F_\pi(Q^2) = F_{u\bar{u}u}(Q^2)$ . Thus there are only three independent form factors,  $F_{u\bar{u}u}(Q^2)$ ,  $F_{u\bar{s}u}(Q^2)$ , and  $F_{u\bar{s}\bar{s}}(Q^2)$ . With this model we have demonstrated explicitly that the impulse approximation is indeed independent of the unphysical parameter  $\eta$  and satisfies current conservation, provided that complete representations of the Dirac matrix

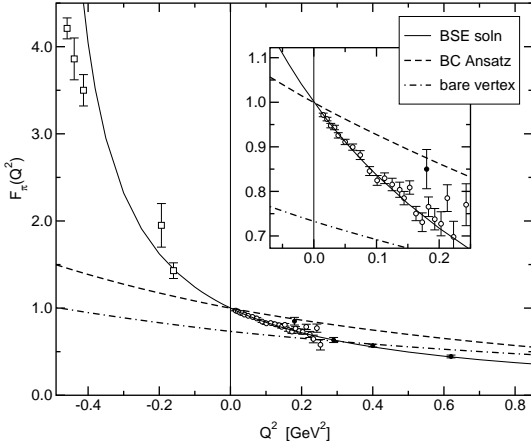


**Figure 4:** The pion charge form factor  $F_\pi(Q^2)$  as obtained from different treatments of the quark-photon vertex. The inset shows the  $Q^2$  region relevant for the charge radius. The data correspond to  $|F_\pi|$ , taken from Refs. [26] (circles), [27] (squares), and [28] (dots).

structure and the  $k \cdot P$  dependence are used [11]. However, with the leading terms in the Chebyshev expansion of the BSAs and the quark-photon vertex given in Eq. (2.5) only, current conservation is violated, and the results do depend on the momentum routing in the loop integral. Including terms up to order  $(k \cdot P)^3$  in this expansion restores current conservation and the independence of the momentum routing to within the numerical accuracy which we estimate to be around 1%. Higher order terms do not change the results more than 1%, at least not at the values of  $Q^2$  we have considered. Also a truncation of the BSAs or the quark-photon vertex in terms of their Dirac amplitudes ( $E$ ,  $F$ ,  $G$ , and  $H$  for the pseudoscalar mesons, and eight transverse amplitudes for the quark-photon vertex) generally leads to a violation of current conservation and/or independence of the choice of integration variable.

In Fig. 4 we show our results for the pion form factor [10] around  $Q^2 = 0$ . With dressed propagators, the use of a bare quark-photon vertex in Eq. (4.4) clearly violates electromagnetic current conservation and leads to  $F_\pi(0) \neq 1$ . Use of the Ball–Chiu Ansatz [29] for the dressed quark-

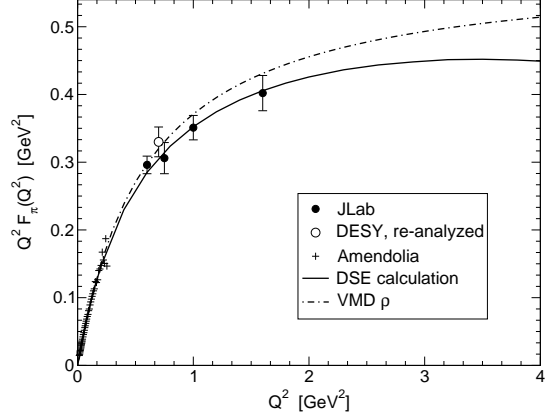


**Figure 5:** Our results for the pion charge form factor [11] compared to new data from JLab [30] including a re-analysis of older data.

photon vertex conserves the electromagnetic current and ensures  $F(Q^2 = 0) = 1$ . However, the behavior of the form factor away from  $Q^2 = 0$  is not constrained by current conservation, and in the present model, use of the Ball–Chiu Ansatz leads to a value for  $r_\pi^2$  which is about 50% too small [10]. With the quark-photon vertex produced by solution of the ladder BSE, and with quark propagators from the rainbow DSE, all constraints from current conservation are satisfied and the calculated value of  $r_\pi^2$  is within 5% of the experimental value [10]. Since the impulse approximation omits meson loop mechanisms such as pion rescattering, previously estimated to add up to 15% to the charge radius [25], the precision of the agreement shown in Fig. 4 should be considered preliminary until these aspects are investigated within the present model.

In Fig. 5 we show our results for  $Q^2 F_\pi(Q^2)$  on a larger  $Q^2$ -domain [11]. We obtain an excellent description of the spacelike  $Q^2$  data, including the latest JLab results, without any adjustment of the model parameters. Our result on this  $Q^2$  domain can quite well be described by a simple monopole, with a mass slightly lower than  $m_\rho$ .

The obtained charged kaon form factor is also in good agreement with the available data, see Fig. 6. The behavior of  $F_K$  on a larger spacelike  $Q^2$ -domain anticipated for future JLab [33]



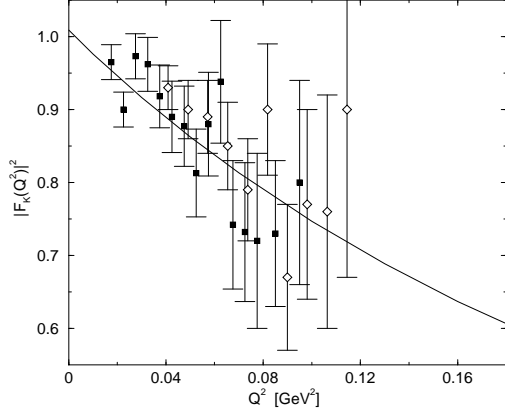


**Figure 6:** The calculated  $K^+$  form factor compared to the data from Refs. [31] (open diamonds) and [32] (solid squares). Within numerical errors,  $F_{K^+}(0) = 1$ .

radii	experiment	calculated
$r_\pi^2$	$0.44 \pm 0.01 \text{ fm}^2$	$0.45 \text{ fm}^2$
$r_{K^+}^2$	$0.34 \pm 0.05 \text{ fm}^2$	$0.38 \text{ fm}^2$
$r_{K^0}^2$	$-0.054 \pm 0.026 \text{ fm}^2$	$-0.086 \text{ fm}^2$

**Table 2:** Our results for the charge radii, compared with the experimental values given in Refs. [28,32,34].

data, is discussed elsewhere [11]. The obtained charge radii for the pion and both the neutral and charged kaons are presented in Table 2, and agree well with the experimental data. These charge radii are somewhat larger than those obtained in a previous study [35] that was framed in terms of semi-phenomenological representations for the confined quark propagators and the BSAs within the impulse approximation. The main difference with that work is that here we use numerical solutions of truncated DSEs for all the elements needed in Eq. (4.4), and that all our parameters were fixed previously.

#### 4.5 Timelike behavior

Experimentally,  $F_\pi(Q^2)$  shows a resonance peak at  $Q^2 = -m_\rho^2$  (in Euclidean metric,  $Q^2 < 0$  corresponds to the timelike region). In general, for timelike photon momenta  $Q^2$  in the vicinity of a vector meson mass-shell, the pseudoscalar meson charge form factor  $F_P(Q^2)$  will exhibit a resonance

peak associated with the propagation of intermediate state vector mesons followed by the decay  $V \rightarrow PP$ . That is [10]

$$F_P(Q^2) \rightarrow \frac{g_{VPP} m_V^2}{g_V (Q^2 + m_V^2 - im_V \Gamma_V)}. \quad (4.13)$$

Here  $m_V^2/g_V$  is the  $V$ - $\gamma$  coupling strength fixed by the  $V \rightarrow e^+ e^-$  decay,  $g_{VPP}$  is the coupling constant for the  $V \rightarrow PP$  decay, and  $\Gamma_V$  is the  $V$  meson width, which is dominated by the latter process.

This vector meson mechanism in the charge form factors of the pion and kaon is generated by the pole structure in the quark-photon vertex exhibited in Eq. (4.7); the relationship of the electroweak decay constant  $f_V$  in Eq. (4.7) with  $g_V$  is  $f_\rho m_\rho = \sqrt{2} m_\rho^2 / g_\rho$  for the  $\rho^0$ , and  $f_\phi m_\phi = 3 m_\phi^2 / g_\phi$  for the  $\phi$  [12]. In the present study, the pole is at a real timelike value of  $Q^2$  since the ladder truncation of the BSE kernel does not generate a width for any meson bound state. For example, one would have to supplement the ladder BSE kernel with the intermediate state  $\pi\pi$  production mechanism to produce a width for the corresponding  $\rho$ -meson resonance in the vertex beyond the threshold for pion production,  $Q^2 < -4 m_\pi^2$  in the timelike region.

Our results shown in Fig. 7 indeed indicate poles at  $Q^2 = -0.55 \text{ GeV}^2$  in the two form factors involving  $\bar{u}\gamma u$  coupling and a pole at  $Q^2 = -1.1 \text{ GeV}^2$  in the form factor involving  $\bar{s}\gamma s$  cou-

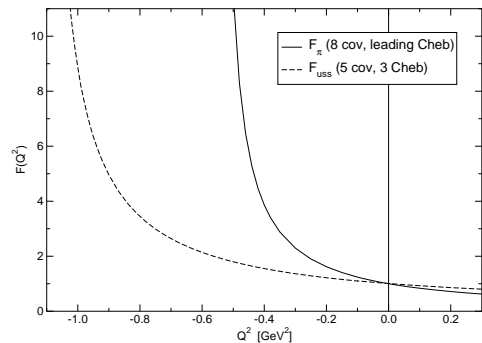


**Figure 7:** Timelike behavior of the individual form factors that make up the pion and kaon charge form factors.

	experiment	theory
$g_{\rho\pi\pi}$	$6.02 \pm .05$	5.4
$g_{\phi KK}$	$4.64 \pm .14$	4.3

**Table 3:** Coupling constants for vector meson strong decays extracted from timelike charge form factors.

pling. These are the  $\rho$  and  $\phi$  respectively and the coupling constants  $g_{\rho\pi\pi}$  and  $g_{\phi KK}$  can be extracted from a fit of Eq. (4.13) to the calculated timelike charge form factors. The results are given in Table 3, and agree reasonably well with experiment. The theoretical or experimental width is a significantly greater fraction of the  $\rho$  mass than it is of the  $\phi$  mass. Thus the omission of meson loops in the BSE kernel can be expected to lead to greater error in the  $\rho$  BS amplitude than in the  $\phi$  BS amplitude. For this reason we speculate that this is also the likely explanation of why the present impulse approximation for  $g_{\rho\pi\pi}$  is further from experiment than the corresponding result for  $g_{\phi KK}$ .

#### 4.6 The $\gamma^*\pi\rho$ and $\gamma^*\pi\gamma$ form factors

The  $\pi^0 \rightarrow \gamma\gamma$  decay rate is dictated by the axial anomaly as prescribed by electromagnetic gauge invariance and chiral symmetry. The resulting invariant amplitude, for photon helicities  $\lambda_1$  and  $\lambda_2$ , is

$$\mathcal{M}^{\lambda_1\lambda_2} = \frac{2i\alpha_{\text{em}}g_{\pi\gamma\gamma}}{\pi\tilde{f}_\pi} \times \epsilon_{\mu\nu\alpha\beta}\epsilon_\mu^{(\lambda_1)}\epsilon_\nu^{(\lambda_2)}k_{1\alpha}k_{2\beta}, \quad (4.14)$$

where  $\epsilon_\mu^{(\lambda_i)}$  and  $k_i$  are the polarization vector and momentum of the  $i^{\text{th}}$  photon, and  $\alpha_{\text{em}}$  is the electromagnetic fine structure constant  $e^2/4\pi$ . As indicated in Eq. (4.14), this result is conventionally expressed in terms of  $\tilde{f}_\pi = f_\pi/\sqrt{2}$ , the pion decay constant in the convention where its value is 92 MeV, rather than the convention  $f_\pi = 131$  MeV used throughout this present work. The coupling constant  $g_{\pi\gamma\gamma}$  appearing in Eq. (4.14) has the chiral limit value  $g_{\pi\gamma\gamma}^0 = 1/2$  and the resulting invariant amplitude for  $\pi^0\gamma\gamma$  coupling saturates the axial anomaly through the massless pion pole in the divergence of the axial current as coupled

to the electromagnetic field. The resulting decay width

$$\Gamma_{\pi^0\gamma\gamma} = \frac{(g_{\pi\gamma\gamma}^0)^2\alpha_{\text{em}}^2m_\pi^3}{16\pi^3\tilde{f}_\pi^2}, \quad (4.15)$$

is within 2% of the experimental width of 7.8 eV. The corrections due to finite pion mass are small.

It is known that these features of the axial anomaly are preserved by the ladder-rainbow truncation of the DSEs combined with an impulse approximation for the  $\pi^0\gamma\gamma$  vertex because the relevant manifestations of electromagnetic gauge invariance and chiral symmetry are present [24,36].

It is convenient to separate out the photon polarization vectors so that we deal with the vertex  $\Lambda_{\mu\nu}^{\gamma\pi\gamma}$  defined by  $\mathcal{M}^{\lambda_1\lambda_2} = \epsilon_\mu^{(\lambda_1)}\Lambda_{\mu\nu}^{\gamma\pi\gamma}\epsilon_\nu^{(\lambda_2)}$ . Corresponding to the flavor decomposition  $\pi^0 = (u\bar{u} - d\bar{d})/\sqrt{2}$ , the impulse approximation or triangle diagram for the vertex has the flavor decomposition

$$\Lambda_{\mu\nu}^{\gamma\pi\gamma}(k_1; k_2) = (\hat{Q}_u^2\Lambda_{\mu\nu}^u - \hat{Q}_d^2\Lambda_{\mu\nu}^d)/\sqrt{2}, \quad (4.16)$$

where  $\hat{Q}_{u/d}$  are the quark charges. We use isospin symmetry where  $\Lambda_{\mu\nu}^u = \Lambda_{\mu\nu}^d$ . For each of these vertices there are two permutations of the final state photons to be included. The resulting expression is<sup>2</sup>

$$\Lambda_{\mu\nu}^{\gamma\pi\gamma}(k_1; k_2) = \frac{\sqrt{2}N_c}{3} \int_q^\Lambda \text{tr}_s [S(q)\Gamma^\pi(q, k)S(k) \times i\Gamma_\mu^\gamma(k, p)S(p)i\Gamma_\nu^\gamma(p, q)]. \quad (4.17)$$

Here the momenta  $p, k$  are determined in terms of the integration momentum  $q$  and the outgoing external momenta  $k_1, k_2$  by momentum conservation.

To conveniently describe the  $\gamma^*\pi\gamma$  transition and define the associated form factor, we replace  $k_1$  by the virtual photon momentum  $Q$  and express  $k_2$  as  $k_2 = P - Q/2$  where the incoming pion momentum is  $P + Q/2$ . Thus the new independent external momenta are  $P$  and  $Q$  and this facilitates

<sup>2</sup>The prefactor in Eq. (4.17) is different than that in Refs. [37,38] because a) the BSE normalization conventions are different and b) the symmetry factor of 2 from the identity of the decay photons is here included in the vertex.

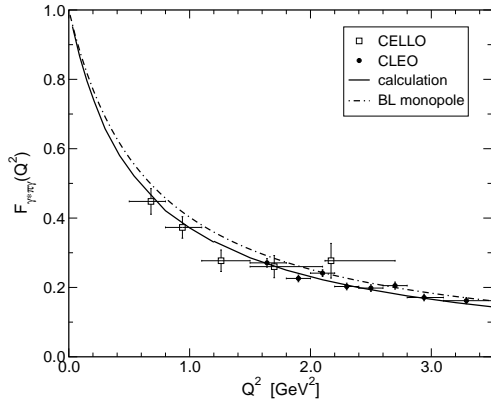


**Figure 8:** The  $\gamma^* \pi \gamma$  form factor [38], with data from CLEO and CELLO [40].

comparisons with our descriptions of meson elastic vertices and form factors. With one virtual photon, the general form of the vertex is

$$\Lambda_{\mu\nu}^{\gamma\pi\gamma}(P, Q) = \frac{2i\alpha_{\text{em}}g_{\rho\pi\gamma}}{\pi\tilde{f}_\pi} \epsilon_{\mu\nu\alpha\beta} P_\alpha Q_\beta \times F_{\gamma^*\pi\gamma}(Q^2), \quad (4.18)$$

where the defined form factor satisfies  $F(0) = 1$ .

The present model produces the coupling constant shown in Table 4 at the physical pion mass; the chiral limit value is essentially the same within numerical accuracy. Our result [38,39] for the transition form factor is displayed in Fig. 8. The corresponding transition radius, shown in Table 4, agrees well with the experimental value reported by the CELLO collaboration [40]. For the moderate range of  $Q^2$  displayed in Fig. 8, both the data and our DSE model are close to the monopole shape fitted to the Brodsky–Lepage asymptotic limit [41]  $Q^2 F(Q^2) \sim 4\pi^2 f_\pi^2$  obtained from pQCD in the factorized approximation<sup>3</sup>.

For the radiative decay  $\rho^+ \rightarrow \pi^+ \gamma$ , the photon can radiate from the  $u$ -quark or the  $\bar{d}$ -quark giving

$$\Lambda_{\mu\nu}^{\rho^+\pi^+\gamma} = \hat{Q}_u \Lambda_{\mu\nu}^{u\bar{d},u} + \hat{Q}_{\bar{d}} \Lambda_{\mu\nu}^{u\bar{d},\bar{d}}, \quad (4.19)$$

where  $\Lambda_{\mu\nu}^{u\bar{d},q}$  is the vertex having the indicated quark flavor labelling and containing no charge

<sup>3</sup>This has been converted to the convention  $f_\pi = 131$  MeV used in the present work.

or flavor weights associated with external bosons. With both the  $\rho^0$  and  $\pi^0$  given by  $(u\bar{u} - d\bar{d})/\sqrt{2}$ , the radiative decay  $\rho^0 \rightarrow \pi^0 \gamma$  can be expressed as

$$\Lambda_{\mu\nu}^{\rho^0\pi^0\gamma} = \hat{Q}_u \Lambda_{\mu\nu}^{u\bar{u},u} + \hat{Q}_d \Lambda_{\mu\nu}^{d\bar{d},d}, \quad (4.20)$$

where the radiative contribution from both quark and antiquark of the same flavor have been combined. In the isospin symmetric limit, we have  $\Lambda_{\mu\nu}^{u\bar{u},u} = \Lambda_{\mu\nu}^{d\bar{d},d} = \Lambda_{\mu\nu}^{u\bar{d},u} = -\Lambda_{\mu\nu}^{u\bar{d},\bar{d}}$ , and thus  $\rho^\pm$  and  $\rho^0$  have identical  $\pi\gamma$  radiative decays at this level. In impulse approximation the physical vertex is [37]

$$\Lambda_{\mu\nu}^{\rho\pi\gamma}(P, Q) = \frac{N_c}{3} \int_q^\Lambda \text{tr}_s [S(q) \Gamma^\pi(q, q_+) S(q_+) \times i\Gamma_\mu^\gamma(q_+, q_-) S(q_-) \bar{\Gamma}_\nu^\rho(q_-, q)], \quad (4.21)$$

where  $Q$  is the photon momentum and the  $\rho$  momentum is represented by  $P - Q/2$ . This is completely analogous to Eq. (4.17) for the  $\gamma^* \pi \gamma$  vertex if the on-shell quark-photon vertex is replaced by the  $\rho$  BSA. In fact, if that photon momentum in Eq. (4.17) is continued into the timelike region, an analysis of the  $\rho^0$  pole contribution in the manner discussed in Sec. 4.5 will identify Eq. (4.21) as the  $\gamma^* \pi \rho$  vertex.

The  $\rho \rightarrow \pi\gamma$  coupling constant and the  $\gamma^* \pi \rho$  form factor are identified from the  $\rho\pi\gamma$  vertex according to

$$\Lambda_{\mu\nu}^{\rho\pi\gamma}(P, Q) = \frac{ie g_{\rho\pi\gamma}}{m_\rho} \epsilon_{\mu\nu\alpha\beta} P_\alpha Q_\beta F_{\gamma^*\pi\rho}(Q^2). \quad (4.22)$$

At the photon point we have  $F(0) = 1$  and  $g_{\rho\pi\gamma}$  is the conventional coupling constant associated with the radiative decay width

$$\Gamma_{\rho \rightarrow \pi\gamma} = \frac{\alpha_{\text{em}} g_{\rho\pi\gamma}^2}{24} m_\rho \left(1 - \frac{m_\pi^2}{m_\rho^2}\right)^3. \quad (4.23)$$

The radiative decay  $\omega \rightarrow \pi^0 \gamma$  is given by

$$\Lambda_{\mu\nu}^{\omega\pi\gamma}(k_\pi, k_\gamma) = \hat{Q}_u \Lambda_{\mu\nu}^{u\bar{u},u} - \hat{Q}_d \Lambda_{\mu\nu}^{d\bar{d},d}, \quad (4.24)$$

where, compared to Eq. (4.20), the change in phase of the second term here comes from the phase of the  $d\bar{d}$  component of the  $\omega$ . With

	experiment	theory
$g_{\gamma\pi\gamma}$	$0.501 \pm .018$	0.50
$r_{\gamma\pi\gamma}^2$	$0.42 \pm .04 \text{ fm}^2$	$0.39 \text{ fm}^2$
$\Gamma_{\pi^0 \rightarrow \gamma\gamma}$	$7.8 \pm 0.6 \text{ eV}$	7.8 eV
$g_{\rho\pi\gamma}/m_\rho$	$0.74 \pm .05 \text{ GeV}^{-1}$	$0.69 \text{ GeV}^{-1}$
$\Gamma_{\rho^+ \rightarrow \pi^+\gamma}$	$68 \pm 7 \text{ keV}$	53 keV
$\Gamma_{\rho^0 \rightarrow \pi^0\gamma}$	$102 \pm 25 \text{ keV}$	53 keV
$g_{\omega\pi\gamma}/m_\omega$	$2.32 \pm .08 \text{ GeV}^{-1}$	$2.07 \text{ GeV}^{-1}$
$\Gamma_{\omega \rightarrow \pi^0\gamma}$	$717 \pm 43 \text{ keV}$	479 keV

**Table 4:** Coupling constant, interaction radius and width for the  $\pi^0 \rightarrow \gamma\gamma$  decay along with coupling constants and widths for the indicated vector meson radiative decays.

isospin symmetry, we have  $\Lambda_{\mu\nu}^{\omega\pi\gamma} = \Lambda_{\mu\nu}^{u\bar{u},u}$  and hence  $g_{\omega\pi\gamma}/m_\omega = 3 g_{\rho\pi\gamma}/m_\rho$ .

As Eq. (4.22) shows, it is  $g/m_V$  that is the natural outcome of the theory for the vector radiative decays, and it is this combination that we report in Table 4. We also give the corresponding decay widths. Except for the difference between the decay of the neutral and charged states of the  $\rho$ , which is beyond the reach of the isospin symmetric impulse approximation, the agreement between theory and experiment is within 10%. This is consistent with the other  $\pi$  and  $\rho$  observables obtained from the same model.

The  $\gamma^*\pi\rho$  form factor plays a role in the interpretation of electron scattering data from light nuclei, because the isoscalar meson-exchange current contributes significantly to these processes. In particular our understanding of the deuteron EM structure functions for  $Q^2 \approx 2 - 6 \text{ GeV}^2$  requires knowledge of this form factor [42]. An initial exploratory study [43] of the  $\gamma^*\pi\rho$  vertex within the present framework, but employing phenomenology to a much greater extent, produced a very soft result for the form factor and this is shown in Fig. 9 as the Mitchell–Tandy curve. It was found [42] that the resulting meson exchange current contribution provided a very good description of the elastic deuteron electromagnetic form factors  $A(Q^2)$  and  $B(Q^2)$  in the range  $2 - 6 \text{ GeV}^2$  where such effects are important.

The model under consideration here, based on

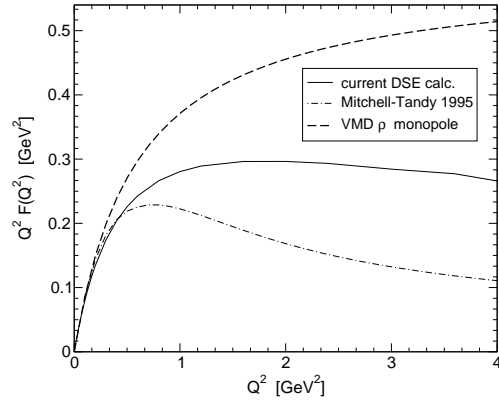


**Figure 9:** The  $\gamma^*\pi\rho$  form factor.

the DSEs of QCD, has no free parameter other than the two set by  $f_\pi$  and  $\langle q\bar{q} \rangle$  as described earlier; the amount of phenomenology is significantly less than the earlier Mitchell–Tandy result [43]. The present work produces a form factor that is much softer than what is inferred from vector meson dominance (VMD) but obviously harder than the Mitchell–Tandy result [43], as can be seen in Fig. 9. We expect the present impulse approximation results for the form factor to be as reliable as the pion and kaon charge form factors from this model [11]. The influence of these recent results upon the analysis of electron scattering from the deuteron remains to be determined. In this regard, some estimation of the likely uncertainty from the virtuality of the  $\pi$  and  $\rho$  within the assumed meson exchange current mechanism needs to be made.

## 5. Extension to finite temperature

The DSE approach can also be used to study QCD at finite temperature. This is done most easily via the Matsubara formalism where the energy components of the 4-momenta become discrete. Thus the quark propagator becomes a function of  $p_n = (\vec{p}, \omega_n)$ , where  $\vec{p}$  is a three-vector, and  $\omega_n = (2n+1)\pi T$  is the fermion Matsubara frequency. The most general decomposition of the dressed renormalised quark propagator now becomes

$$S^{-1}(p_n) = i\vec{\gamma} \cdot \vec{p} A(p_n) + i\gamma_4 \omega_n C(p_n) + B(p_n),$$

$$(5.1)$$

which satisfies the DSE

$$S^{-1}(p_n) = Z_2^A i\vec{\gamma} \cdot \vec{p} + Z_2^C i\gamma_4 \omega_n + Z_4 m(\mu) + \Sigma(p_n), \quad (5.2)$$

with quark self-energy given by

$$\Sigma(p_n) = \frac{4}{3} \int_{q,l}^{\Lambda} g^2 D_{\mu\nu}(k_{n-l}) \gamma_\mu S(q_l) \Gamma_\nu, \quad (5.3)$$

where we have employed the notation

$$\int_{q,l}^{\Lambda} = T \sum_{l=-\infty}^{\infty} \int^{\Lambda} \frac{d^3 q}{(2\pi)^3}. \quad (5.4)$$

Note that the argument of the gluon propagator,  $k_{n-l} = p_n - q_l$ , corresponds to an even (bosonic) Matsubara frequency. For renormalization of the propagator we require

$$S^{-1}(p_0) \Big|_{p^2 + \omega_0^2 = \mu^2} = i\vec{\gamma} \cdot \vec{p} + i\gamma_4 \omega_0 + m(\mu). \quad (5.5)$$

As before, we use the rainbow truncation for the vertex,  $\Gamma_\nu = \gamma_\nu$ , in combination with the ladder truncation for the BSE kernel  $K$ .

### 5.1 Chiral symmetry restoration

Chiral symmetry restoration has been studied at both zero and finite- $(T, \mu)$  in a class of confining DSE models similar to the one discussed in Secs. 3 and 4 [5]. Here, two models are considered in which the long-range part of the interaction is an integrable infrared singularity [44] motivated by  $T = 0$  studies [45] of the gluon DSE. Both models can be described by [13]

$$\begin{aligned} g^2 D_{\mu\nu}(k_m) &= P_{\mu\nu}^L \mathcal{D}(k_m; m_g) + P_{\mu\nu}^T \mathcal{D}(k_m; 0), \\ \mathcal{D}(k_m; m_g) &= 2\pi^2 D \frac{2\pi}{T} \delta_{0j} \delta^3(\vec{k}) \\ &\quad + \mathcal{D}_M(k_m^2 + m_g^2), \end{aligned} \quad (5.6)$$

where  $P_{44}^T = P_{4i}^T = 0$ ,  $P_{ij}^T = \delta_{ij} - k_i k_j / k^2$ ,  $P_{\mu\nu}^L = \delta_{\mu\nu} - k_\mu k_\nu / k_m^2 - P_{\mu\nu}^T$ , and  $m_g$  is a Debye mass. The strength parameter  $D$  is fixed by a fit to  $m_\pi$  and  $f_\pi$  at  $T = 0$ . The models differ in the details of  $\mathcal{D}_M$ .

It is anticipated that the restoration of chiral symmetry, which accompanies the formation of a quark-gluon plasma at nonzero temperature  $T$ , is a second-order phase transition in QCD with 2 light flavors. Such transitions are characterised by two critical exponents:  $(\beta, \delta)$ , which describe the response of the chiral order parameters,  $\mathcal{X}$ , to changes in  $T$  and in the current-quark mass,  $m$ . Denoting the critical temperature by  $T_c$ , and introducing the reduced-temperature  $t := T/T_c - 1$  and reduced mass  $h := m/T$ , then

$$\mathcal{X} \propto (-t)^\beta, \quad t \rightarrow 0^-, h = 0, \quad (5.7)$$

$$\mathcal{X} \propto h^{1/\delta}, \quad h \rightarrow 0^+, t = 0. \quad (5.8)$$

Calculating the critical exponents is an important goal because of the notion of universality, which states that their values depend only on the symmetries and dimensions, but not on the microscopic details of the theory.

One order parameter for dynamical chiral symmetry breaking is the quark condensate [3]  $\langle \bar{q}q \rangle_\mu^0$ . There are other, equivalent order parameters such as

$$\mathcal{X} := B(p = 0, \omega_0), \quad \mathcal{X}_C := \frac{B(p = 0, \omega_0)}{C(p = 0, \omega_0)}. \quad (5.9)$$

They should be equivalent, and the onset of that equivalence is a good way to determine the domain of reduced mass and reduced temperature in which the scaling behavior and critical exponents become manifest. In Ref. [13] it has been verified numerically that in the chiral limit ( $m = 0$ ) and for  $t \sim 0$ :  $f_\pi \propto \langle \bar{q}q \rangle \propto \mathcal{X}(t, 0)$ ; i.e., that these quantities are all indeed bona fide order parameters.

The success of the nonlinear  $\sigma$ -model in describing long-wavelength pion dynamics underlies a conjecture [46] that chiral symmetry restoration at finite  $T$  in 2-flavor QCD is in the same universality class as the 3-dimensional,  $N = 4$  Heisenberg magnet ( $O(4)$  model), with critical exponents [47]  $\beta^H = 0.38 \pm .01$ ,  $\delta^H = 4.82 \pm .05$ . This is to be contrasted with mean-field critical exponents,  $\beta^{\text{mf}} = 0.5$ ,  $\delta^{\text{mf}} = 3$ .

### 5.2 Infrared dominant model

A simple model [44] that is considered in re-

cent work [13,48–50] is the infrared dominant [ID] model with  $\mathcal{D}_M(s) \equiv 0$  in Eq. (5.6), with the mass-scale  $D = 0.56 \text{ GeV}^2$  fixed by fitting  $\pi$ - and  $\rho$ -meson masses at  $T = 0$ . A current-quark mass of  $m = 12 \text{ MeV}$  yields  $m_\pi = 140 \text{ MeV}$ . There are two chiral limit solutions corresponding to two phases: the symmetric Wigner–Weyl solution in which  $B_0(p_n) = 0$ , and the chirally broken Nambu–Goldstone solution in which

$$B_0(p_n) = \begin{cases} \sqrt{2D - 4p_n^2}, & p_n^2 < \frac{D}{2} \\ 0, & \text{otherwise.} \end{cases}$$

From Eq. (5.7), the critical exponent  $\beta$  for chiral restoration is simply  $\beta = 1/2$  and  $T_c = \sqrt{2D}/2\pi \sim 170 \text{ MeV}$ . With a finite current-quark mass the quark DSE becomes a fourth-order algebraic equation and it is straightforward to establish [50] from Eq. (5.8) that  $\delta = 3$ . Clearly, this model has mean field critical exponents. The question is: is this result model-dependent or is it a more general property?

### 5.3 1-loop perturbative QCD for the UV

To provide a more realistic ultraviolet behavior, one can add a short-range term to the  $\delta$ -function, corresponding to the exchange of a perturbative gluon at momenta  $p^2 \gg \Lambda_{\text{QCD}}^2$ . In Ref. [13], chiral symmetry restoration at finite temperature is studied using  $\mathcal{D}_M(s) = \mathcal{G}(s)/s$  in Eq. (5.6) where  $\mathcal{G}$  is given by Eq. (3.3)<sup>4</sup>. Again, the parameters are fixed at  $T = 0$  by requiring a good fit to  $m_{\pi/K}$  and  $f_{\pi/K}$  [3].

The Debye mass is  $m_g^2 = (16/5)\pi^2 T^2$  and two values of the parameter  $\omega$  are used which are phenomenologically equivalent at  $T = 0$ :  $\omega_1 = 0.6m_t$  and  $\omega_2 = 1.2m_t$ . To fix  $m_\pi = 140 \text{ MeV}$ , the former requires a renormalization point invariant current-

<sup>4</sup>Here a combination of a Gaussian function and  $\delta$ -function is used to represent the strength of the interaction at small momenta, whereas in Sec. 4, we used Eq. (3.3) without an additional  $\delta$ -function. Hence the results described here use  $D = 0.78 \text{ GeV}^2$  which is lower than the value  $D = 0.93 \text{ GeV}^2$  of the previous section. Qualitatively, the results are independent of the details of the effective interaction, as long as it is strong enough to break chiral symmetry at  $T = 0$ .

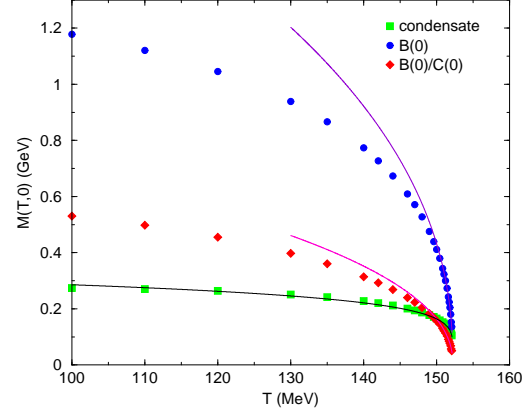


**Figure 10:** The analysis of 3 equivalent order parameters for the critical exponent  $\beta$  within model  $\omega_2$ .

quark mass of  $\hat{m}_u = 6.6 \text{ MeV}$ , while the latter requires  $\hat{m}_u = 5.7 \text{ MeV}$ . The critical temperature can be found from a calculation of the order parameter in the chiral limit,  $\hat{m} = 0$ , as is shown in Fig. 10. Once  $T_c$  is known, one can analyse the behavior of the order parameter as a function of the current mass at  $T = T_c$ , see Fig. 11.

Although one can in principle extract the critical exponents  $\beta$  and  $\delta$  from these plots, a much better method is to use the chiral and thermal susceptibilities [50]. The critical exponents obtained from the susceptibilities [13] are in good agreement with a direct calculation of the critical exponents using Eqs. (5.7) and (5.8), and are

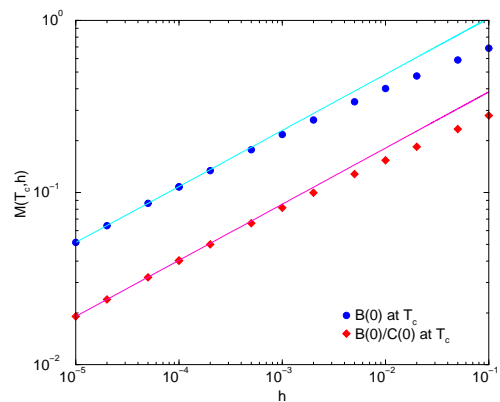


**Figure 11:** The analysis of 2 equivalent order parameters for the critical exponent  $\delta$  within model  $\omega_2$ .

	ID	$\omega_1$	$\omega_2$
$T_c$ (MeV)	169	120	152
$\beta$	$\frac{1}{2}$	0.50	0.50
$\delta$	3	3.00	3.02

**Table 5:** Critical temperature for chiral symmetry restoration and critical exponents characterising the second-order transition in the three illustrative models [13].

given in Table 5. Note that the scaling relations are only valid for very small current-quark masses:  $\log_{10}(\hat{m}/\hat{m}_u) < -5$ , where  $\hat{m}_u$  corresponds to the current-quark mass that gives  $m_\pi = 140$  MeV in this model. It is only in this scaling region that the different order parameters become equivalent. These results are qualitatively, and for the critical exponents quantitatively, independent of the parameters in this model.

## 6. Spatial $\bar{q}q$ modes

At  $T = 0$  the mass-shell condition for a meson as a  $\bar{q}q$  bound state of the BSE is equivalent to the appearance of a pole in the  $\bar{q}q$  scattering amplitude as a function of  $P^2$ . At  $T \neq 0$  in the Matsubara formalism, the  $O(4)$  symmetry is broken by the heat bath and one has  $P \rightarrow (\vec{P}, \Omega_m)$  where  $\Omega_m = 2m\pi T$ . Bound states and the poles they generate in propagators may be investigated through polarization tensors, correlators or Bethe–Salpeter eigenvalues. This pole structure is characterized by information at discrete points  $\Omega_m$  on the imaginary energy axis and at a continuum of 3-momenta. Analytic continuation for construction of real-time Green’s functions (and related propagation properties) has been well-studied [51]. An unambiguous result is obtained by the requirement that the continuation yield a function that is bounded at complex infinity and analytic off the real axis [51]. One may search for poles as a function of  $\vec{P}^2$  thus identifying the so-called spatial or screening masses for each Matsubara mode. These serve as one particular characterization of the propagator and the  $T > 0$  bound states. Here

we discuss the mass dependence of the poles in the zeroth Matsubara mode,  $\Omega_m = 0$ .

### 6.1 Chiral modes near $T_c$

In the Matsubara formalism, the number of coupled equations in the the quark DSE, Eq. (2.1), and the meson BSE, Eq. (2.2), scales up with the number of fermion Matsubara frequencies included. At low temperature, the necessary large number of such modes combined with the loss of  $O(4)$  symmetry entails that a straightforward extension of large scale  $T = 0$  calculations is prohibitive. Meson  $\bar{q}q$  modes at  $T > 0$  have often been studied within the Nambu–Jona-Lasinio model where the contact nature of the effective interaction allows decoupling of the Matsubara modes and analytic summation methods, see for example, Ref. [52] and references therein. However the lack of quark confinement in that model leads to unphysical thresholds for  $\bar{q}q$  dissociation. To learn about the fate of meson modes as influenced by deconfinement and chiral restoration, it is desirable to explore the  $T \neq 0$  properties of models that, at  $T = 0$ , confine quarks and provide a realistic description of the light mesons.

Such a study has recently been carried out [14] within the model of Sec. 5.3. This work was restricted to temperatures near and above the transition,  $T \geq 100$  MeV, where a maximum of 10 Matsubara modes were found to be sufficient; only pseudoscalar and scalar modes were considered. In the chiral limit and at  $T = 0$ , there is dynamical chiral symmetry breaking and thus one finds massless pseudoscalar Goldstone bosons. The lowest scalar bound state in this model is an idealized  $\sigma$ -meson with  $m_\sigma = 0.56$  GeV. Such a low-mass scalar is typical of the rainbow-ladder truncation, although there is some model sensitivity. The rainbow-ladder truncation yields degenerate isoscalar and isovector bound states, and ideal flavor mixing in the 3-flavor case; improvements beyond the ladder truncation are required in order to describe the observed scalar mesons. Furthermore, in the isoscalar-scalar channel, it will be necessary to include couplings to the dominant  $\pi\pi$  mode [53] because of the large  $\sigma$  width. In the absence of

such corrections, the  $\sigma$  properties discussed below are those of an idealized chiral partner of the  $\pi$ .

The poles in the 0th Matsubara modes of the scalar and pseudoscalar vertices,  $\Gamma_S(p_n, k_n; \vec{P}, 0)$  and  $\Gamma_{PS}(p_n, k_n; \vec{P}, 0)$  where  $\vec{P} = \vec{p} - \vec{k}$ , evolve with  $T$  such that at the critical temperature, one has degenerate, massless scalar and pseudoscalar bound states [14]. Above  $T_c$ , these bound states persist, becoming increasingly massive with increasing  $T$ . Furthermore, all but the leading Dirac amplitude vanish above  $T_c$  and the surviving pseudoscalar amplitude  $E_\pi$  is pointwise identical to the surviving scalar one. These results indicate that the chiral partners are locally identical above  $T_c$ , they do not just have the same mass. Approaching  $T_c$  from below, the  $\sigma$  mass behaves as  $m_\sigma \propto (1 - T/T_c)^\beta$  within numerical errors. Note that this is the same behavior as the chiral condensate and other, equivalent order parameters for chiral symmetry restoration, such as the decay constant  $f_\pi$ , as discussed in the previous section. For nonzero current-quark masses chiral symmetry restoration is exhibited as a crossover rather than a phase transition, see Fig. 12. The  $\sigma$  mass exhibits a dip around the phase transition. The scalar and pseudoscalar meson masses become indistinguishable at  $T \sim 1.2 T_c$ .

With the BSAs obtained from the homogeneous BSE, one can now calculate the  $T$ -

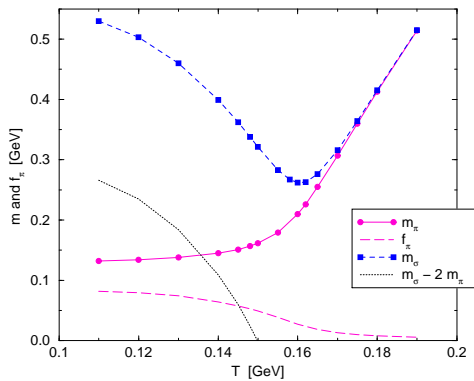


**Figure 12:** The  $T$ -dependence of  $m_\pi$  and  $f_\pi$  along with the mass of the scalar chiral partner of the pion (adapted from Ref. [14]). The model used is  $\omega_2$ , see Table 5 and Sec 5.3.

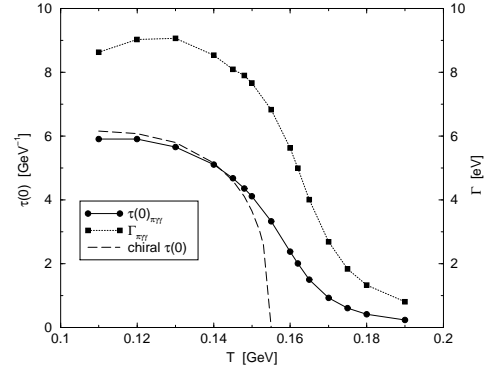


**Figure 13:**  $T$ -dependence of the coupling  $\mathcal{T}(0)$  and the  $\pi^0 \rightarrow \gamma\gamma$  width (adapted from Ref. [14]).

dependence of other meson properties [14]. The decay of a pion into two photons is calculated in a similar fashion as at  $T = 0$  in the previous section. Using the Ball–Chiu Ansatz [29] for the photon vertices, one can analytically show that in the chiral limit the pseudoscalar piece ( $E_\pi$ ) of the pion BSA [36] saturates the Abelian anomalous contribution to the divergence of the axial-vector vertex:  $g_{\pi\gamma\gamma} = \frac{1}{2}$ . The tensor structure of Eq. (4.21) survives at nonzero temperature<sup>5</sup>

$$\Lambda_{i4}(k_1, k_2) = \frac{\alpha_{\text{em}}}{\pi} (\vec{k}_1 \times \vec{k}_2)_i \mathcal{T}(0), \quad (6.1)$$

where  $k_1$  and  $k_2$  are the photon momenta (or rather, the spatial components of the zeroth Matsubara modes of the photons), and with  $\mathcal{T}(0) = g_{\pi\gamma\gamma} F(0)/f_\pi$ . With a suitable extension of the Ball–Chiu Ansatz to nonzero temperature one can determine the  $T$  dependence of the coupling constant  $g_{\pi\gamma\gamma}$ , or rather, of  $g_{\pi\gamma\gamma}/f_\pi$  which is the more interesting quantity.

The  $T$ -dependence of the  $\pi^0\gamma\gamma$  coupling and the associated width is depicted in Fig. 13. Clear in the figure is that  $\mathcal{T}(0)$  vanishes at  $T_c$ ; in fact, it vanishes with the same critical exponents as the other order parameters:  $\beta = 0.5$ , indicating mean field behavior [14]. An accurate calculation of the critical exponent is possible because the Goldberger–Treiman-like relation [9]  $f_\pi^0 E_\pi(p_n) = B_0(p_n)$  is satisfied for all  $T$ . It is therefore not nec-

<sup>5</sup>In this section we use the convention  $f_\pi = 92$  MeV.



essary to solve the BSE for the chiral pion bound state amplitude  $E_\pi$ . Thus, in the chiral limit, the coupling to the dominant decay channel closes for both charged *and* neutral pions. These features were anticipated in Ref. [46]. Further, the calculated  $\mathcal{T}(0)$  is monotonically decreasing with  $T$ , supporting the perturbative analysis to order  $(T^2/f_\pi^2)$  in Ref. [54]. For  $\hat{m} \neq 0$  both the coupling:  $g_{\pi^0\gamma\gamma}/f_\pi$ , and the width exhibit the crossover with a slight enhancement in the width as  $T \rightarrow T_c$  due to the increase in  $m_\pi$ .

The isoscalar-scalar- $\pi\pi$  strong coupling vanishes at  $T_c$  in the chiral limit, which can be traced to  $B_{\text{chiral}} \rightarrow 0$ . For  $\hat{m} \neq 0$ , the coupling reflects the crossover. For the present case of the idealized  $\sigma$ -meson, there are no physical consequences because the width for the decay  $\sigma \rightarrow \pi\pi$  vanishes just below  $T_c$  where the  $\sigma$  meson mass falls below  $2m_\pi$  and the phase space factor vanishes.

## 6.2 Separable model

For studies at low finite temperature, where continuity with  $T = 0$  results is to be verified, the required number of Matsubara modes can be of order  $\sim 10^3$ . This is rather cumbersome with the model discussed above, but can be done if one utilizes a separable Ansatz [15,56] for the interaction that can implement the essential qualitative features of DSE/BSE models at finite temperature. Separable representations have previously been found capable of an efficient modeling of the effective  $\bar{q}q$  interaction in the infrared domain for  $T = 0$  meson observables [57,58].

In Ref. [15] a simple separable interaction is used, which confines quarks at  $T = 0$ . The few parameters are fixed by  $\pi$  and  $\rho/\omega$  properties. The approach is a simplification of one developed earlier [58] that was found to be quite successful for the light meson spectrum at  $T = 0$ . The confining mechanism is an infrared enhancement in the quark-quark interaction that is strong enough to remove the possibility of a mass shell pole in the quark propagator for real  $p^2$ . In this implementation, it is particularly transparent that sufficiently high temperature will necessarily restore a quark mass-shell pole and there will be a deconfinement

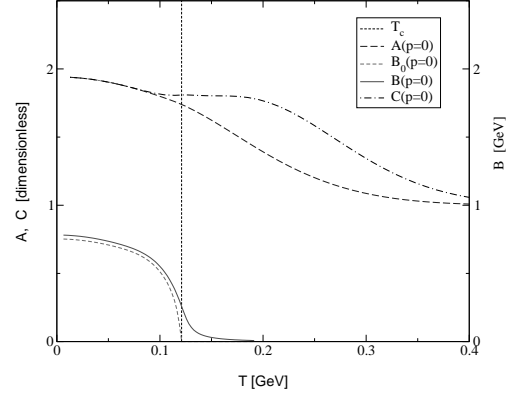


**Figure 14:**  $T$ -dependence of quark self-energy amplitudes at  $p = 0$  (adapted from Ref. [15]).

transition. This model also implements low temperature dynamical chiral symmetry breaking and it preserves the Goldstone theorem in that the generated  $\pi$  is massless in the chiral limit. The solutions of the BSE for the  $\pi$  and  $\rho$  modes are particularly simple and are used to study the  $T$ -dependence of the meson masses and decay constants in the presence of both deconfinement and chiral restoration mechanisms.

Here we discuss the results obtained [15] with the rank-2 separable interaction

$$\begin{aligned}
 D_{\mu\nu}^{\text{eff}}(p-q) = & \delta_{\mu\nu} [D_0 f_0(p^2)f_0(q^2) \\
 & + D_1 f_1(p^2)(p \cdot q)f_1(q^2)], \quad (6.2)
 \end{aligned}$$

and a Feynman-like gauge is chosen for phenomenological simplicity. The choice for the two strength parameters  $D_0, D_1$ , and corresponding form factors  $f_i(p^2)$  is constrained by consideration of the resulting solution of the DSE for the quark propagator in the rainbow approximation, and fitted to reproduce  $\pi$  and  $\rho$  properties at  $T = 0$ . In Ref. [15] a single Gaussian representation for the  $f_i(p^2)$  was used to represent the major features. The finite  $T$  extension is implemented using the Matsubara formalism as before, via the discretization of the timelike component of momenta:  $p \rightarrow p_n = (\vec{p}, \omega_n)$ .

The  $T$ -dependence of the solutions for  $A, B$  and  $C$  at  $\vec{p}^2 = 0$  is displayed in Fig. 14. The results shown are for the lowest Matsubara mode ( $\omega_0 = \pi T$ ) which provides the leading behavior

as  $T$  is increased. The chiral restoration critical temperature  $T_c = 121$  MeV is identified from the vanishing of the chiral limit amplitude  $B_0(0, \omega_0)$  as shown. Below  $T_c$ ,  $A$  and  $C$  are relatively constant,  $O(4)$  symmetry is approximately manifest, and the main effect is an almost constant quark wave function renormalization via  $1/C$ ; the central feature is a rapidly decreasing mass function<sup>6</sup>. Above  $T_c$ , there remains a significant temperature range where the self-interaction effects are strong, both  $A$  and  $C$  are considerably enhanced above their perturbative values, and the breaking of  $O(4)$  symmetry is manifest. The present model thus captures the qualitative  $T$ -dependence observed for the dressed quark propagator in studies of the quark DSE [50,59].

The deconfinement transition is characterized by the appearance of a quark propagator pole for real values of  $\vec{p}^2$ . The chiral restoration point  $T_c$  and the quark deconfinement point  $T_d$  are generally expected to be identical or nearly so [60]. The separable model under consideration here produces  $T_d = 0.9 T_c = 105$  MeV.

### 6.3 Vector mesons at nonzero $T$

Due to the breaking of  $O(4)$  invariance, the  $T = 0$  transverse vector meson splits for  $T > 0$  into 3-space longitudinal and transverse modes. For the spatial modes characterized by  $(\vec{P}, \Omega_0 = 0)$ , the BSAs studied in the separable model are [15]

$$\Gamma_\mu^{\rho(L)}(p_n, k_n; \vec{P}) = \delta_{\mu 4} \gamma_4 f_0(q_n^2) F_{\rho(L)}(\vec{P}^2), \quad (6.3)$$

and

$$\Gamma_i^{\rho(T)}(p_n, k_n; \vec{P}) = \left( \gamma_i - \frac{P_i \vec{P} \cdot \vec{\gamma}}{\vec{P}^2} \right) f_0(q_n^2) F_{\rho(T)}(\vec{P}^2), \quad (6.4)$$

where  $q_n = (p_n + k_n)/2$  is the relative momentum. The  $T$ -dependence of the corresponding masses is displayed in Fig. 15. These modes are almost degenerate and  $T$ -independent until

<sup>6</sup>The rank-1 limit of this model has  $A = C = 1$  for all  $T$  and the behavior of  $B(0, \omega_0)$  as function of  $T$  is similar to that in Fig. 14 except  $T_c = 146$  MeV is obtained [15].

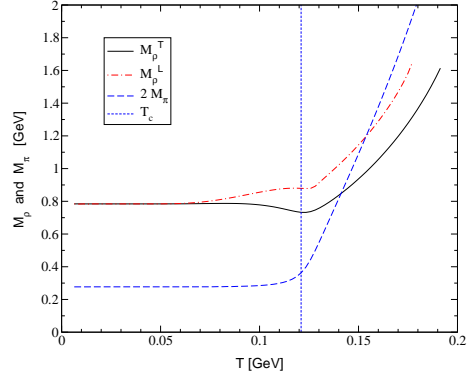


**Figure 15:**  $T$ -dependence of the longitudinal  $\rho$  mass (dot-dashed line) and the transverse  $\rho$  mass (solid line). Also shown is  $2M_\pi$  indicating that the strong decay channel becomes inaccessible within 20-30 MeV beyond  $T_c$  (adapted from Ref. [15]).

about  $T_c/2$  where the breaking of  $O(4)$  invariance becomes significant. The qualitative features  $M_\rho^L(T) > M_\rho^T(T)$  and  $M_\rho^T(T) \approx \text{constant}$  for  $T < T_c$  seen here in the context of a finite range interaction have previously been noted within the limiting case of the zero momentum range ID model [49]. This latter model was not studied for  $T > T_c$ . In the separable model discussed here, the longitudinal mode becomes unstable to  $\bar{q}q$  dissociation at  $T \sim 180$  MeV; the transverse mode continues to be below the spatial  $\bar{q}q$  threshold for the temperature range displayed.

Next, one can study the couplings appropriate to  $\rho^0 \rightarrow e^+ e^-$  and  $\rho \rightarrow \pi\pi$  for the meson modes characterized by  $P = (\vec{P}, 0)$  [15]. The various spatial modes from  $\Omega_m \neq 0$  are characterized by masses much greater than that of the lowest mode considered here. It is anticipated that this lowest mode characterizes the qualitative behavior of the physical decay processes  $\rho^0 \rightarrow e^+ e^-$  and  $\rho \rightarrow \pi\pi$ .

The  $T = 0$  expression for the electromagnetic coupling constant  $g_\rho$  has a straightforward extension to  $T > 0$  for a transverse spatial  $\rho^0$  mode [15]. Use of the  $\Omega_m = 0$  solution described above yields

$$\frac{M_\rho^{T^2}(T)}{g_\rho(T)} =$$

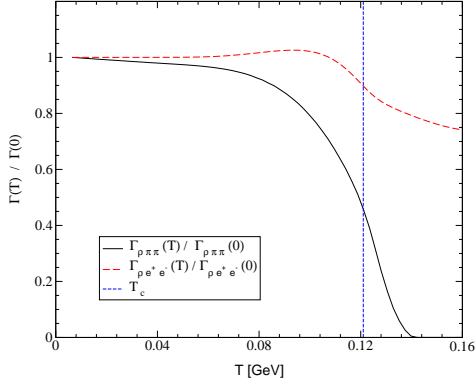


**Figure 16:**  $T$ -dependence of the transverse  $\rho$  partial widths due to electromagnetic  $e^+e^-$  decay (dashed line) and strong  $\pi\pi$  decay (solid line) (adapted from Ref. [15]).

$$\frac{N_c}{2} \int_{q,n}^{\Lambda} \text{tr}_s [\gamma_i S(q_{n+}) \Gamma_i^{\rho(T)}(q_{n+}, q_{n-}; \vec{P}) S(q_{n-})]. \quad (6.5)$$

The impulse approximation for the  $\rho\pi\pi$  vertex [4,37], after extension to  $T > 0$  for spatial modes characterized by  $Q = (\vec{Q}, 0)$  for the  $\rho$  and  $P = (\vec{P}, 0)$  for the relative  $\pi\pi$  momentum, takes the form

$$\begin{aligned} \Lambda_\nu(P, Q) &= P_\nu g_{\rho\pi\pi}(T) = \\ &-2N_c \int_{q,n}^{\Lambda} \text{tr}_s [S(q) \Gamma_\pi(q, q_{n+}; -\vec{P}_+) S(q_{n+}) \\ &\times \Gamma_\nu^{\rho(T)}(q_{n+}, q_{n-}; \vec{Q}) S(q_{n-}) \Gamma_\pi(q_{n-}, q; \vec{P}_-)], \end{aligned} \quad (6.6)$$

where  $\vec{P}_\pm = \vec{P} \pm \vec{Q}/2$ . Use of Eq. (6.3) immediately shows that the longitudinal  $\rho$  mode cannot couple to  $\pi\pi$ . With summation over enough Matsubara modes for convergence, both the electromagnetic coupling  $g_\rho(T)$ , and the strong coupling  $g_{\rho\pi\pi}(T)$ , reproduce the independently determined  $T = 0$  results of this model. There is very little  $T$ -dependence below about  $0.8 T_c$  where there is approximate  $O(4)$  symmetry as evident in the quark propagator behavior in Fig. 14. Near  $T_c$ ,  $g_\rho(T)$  rises and  $g_{\rho\pi\pi}(T)$  decreases.

Combined with the relevant phase space, this

leads to the electromagnetic decay width

$$\Gamma_{\rho^0 \rightarrow e^+ e^-}(T) = \frac{4\pi \alpha M_\rho^T(T)}{3 g_\rho^2(T)}, \quad (6.7)$$

while the corresponding strong decay width is

$$\Gamma_{\rho \rightarrow \pi\pi}(T) = \frac{g_{\rho\pi\pi}^2(T) M_\rho^T(T)}{4\pi \cdot 12} \left[ 1 - \frac{4M_\pi^2(T)}{M_\rho^T(T)} \right]^{3/2}. \quad (6.8)$$

The  $T$ -dependence estimated in this way for the decay widths is due to the response of the quark substructure to the heat bath, particularly the restoration of chiral symmetry. The results are displayed in Fig. 16. The contrast between the behavior of the electromagnetic and strong widths near and just above  $T_c$  should be a more robust finding than the details of the individual processes. The strong width decreases rapidly and vanishes just above  $T_c$  while the electromagnetic width remains within 20% of the  $T = 0$  value. Part of the strong decrease of the intrinsic  $\pi\pi$  width of the transverse  $\rho$  is due to the decrease in the coupling constant, however the dominant effect is the  $T$ -dependence of the phase space factor in Eq. (6.8). As displayed in Fig. 15,  $2M_\pi(T)$  rises faster with  $T$  than does  $M_\rho^T(T)$  until at  $T = 1.17 T_c$  one has  $M_\rho^T = 2M_\pi$ . Beyond this point, the strong decay  $\rho^T \rightarrow \pi\pi$  is phase-space blocked. This suggests that the total  $\rho^T$  width of 151 MeV at  $T = 0$  decreases by about 50% near  $T = T_c$  and drops sharply to the electromagnetic value of about 6 keV by  $T = 1.17 T_c$ .

One would expect the mass of the pseudoscalar  $K$  correlation to rise with  $T$  in a similar fashion to  $M_\pi$ , while the masses of the vector  $\phi$  and  $K^*$  modes should rise like the  $\rho$ . This suggests that the vector modes  $\rho$ ,  $K^*$  and  $\phi$  tend to be trapped with their relatively long electroweak lifetimes and with significantly increased masses for a domain of high temperatures above the transition. This suggests that within the gas of pions and other pseudoscalars that dominate the hot hadronic product from heavy-ion collisions, the role of vector meson correlations in producing the dilepton spectra could be significantly less than conventional expectations.

This narrowing of the intrinsic decay width of the vector meson mode in the heat bath, and also the decrease of the decay width of the idealized  $\sigma$ -meson discussed in Sec. 6.1, is a mechanism that is distinct from the collisional broadening effect [61] from the many-hadron environment. The results discussed here indicate that there is a non-trivial  $T$ -dependence to intrinsic coupling constants, such as  $g_{\rho\pi\pi}$  and  $g_{\sigma\pi\pi}$ , and decay phase space. The intrinsic effect tends to significantly decrease the decay width; the hadronic medium effects have the opposite influence. An approach that incorporates both phenomena is clearly called for.

Also note that only the spatial or screening  $\bar{q}q$  masses have been investigated within this model. The temporal masses provide a different characterization of the correlations; lattice simulations indicate that spatial masses become much larger than the temporal masses above  $T_c$  [55], whereas a Nambu–Jona-Lasinio model study [52] found that they are significantly different only in the range  $150 \text{ MeV} < T < 350 \text{ MeV}$ .

#### 6.4 Behavior at high $T$

Above the deconfinement and chiral transition temperature, it might be expected that meson modes should dissolve in favor of a gas of essentially massless quarks. However for a significant temperature range above  $T_c$ , the spatial  $\pi$  and  $\rho$  modes studied here continue to be stable against  $\bar{q}q$  dissociation and do not dissolve into a free quark gas [15]. The results for  $M_\pi(T)$  and  $M_\rho^T(T)$  are displayed in Fig. 17, along with the quark dynamical mass function at  $p = 0$ , using the simpler rank-1 separable interaction. The masses of both spatial meson modes approach the asymptotic behavior  $2\pi T$  from below. This asymptotic behavior has been observed in lattice simulations [60,62] as well.

The emergence of the  $2\pi T$  behavior for masses of  $\bar{q}q$  correlations at large  $T$  can easily be understood in the rank-1 model, as is shown in Ref. [15]. There it is found that for spatial meson modes  $M(T) \sim 2\pi T - \Delta(T)$  where  $\Delta$  is a positive mass defect that will typically decrease with  $T$ . Thus the spatial meson mass or screening mass will ap-

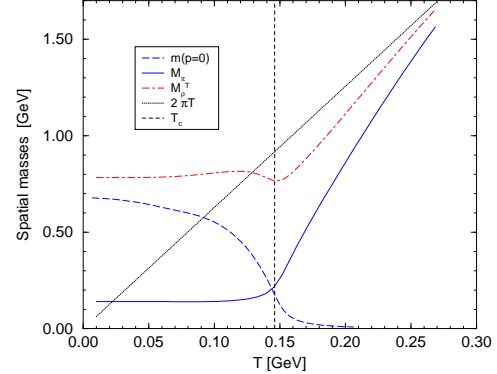


**Figure 17:** High  $T$  behavior of the spatial masses of the  $\pi$  and transverse  $\rho$  modes from the rank-1 separable model (adapted from Ref. [15]).

proach the thermal mass of a pair of massless fermions from below.

The same qualitative behavior at large  $T$  can be seen in a semi-analytic way by considering the ID model of Sec. 5.2. For example, it is found [15] that the leading large  $T$  behavior of  $M_\rho^T(T)$  is

$$M_\rho^{T^2}(T) \rightarrow (2\pi T)^2 \left(1 - \frac{\eta}{\pi T} \dots\right). \quad (6.9)$$

Due to the long range nature of this model, the asymptotic spatial mass defect of the transverse  $\rho$  mode actually becomes constant  $\Delta_\rho(T) \rightarrow \eta$ .

In Fig. 18 the  $\pi$  and transverse  $\rho$  spatial masses at  $T > T_c$  from both the rank-1 separable model and the ID model are presented in comparison with lattice QCD simulations of spatial screening

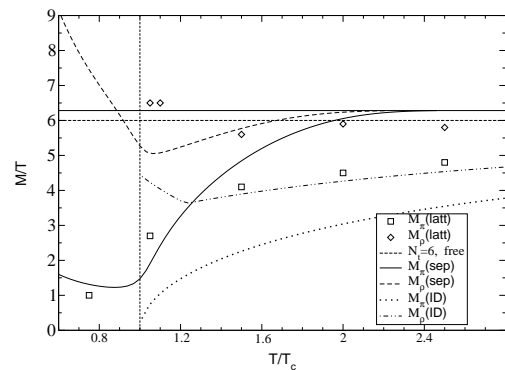


**Figure 18:** Spatial masses from the rank-1 separable model (sep) and the ID model from Ref. [15] compared to lattice QCD simulations (latt) taken from Ref. [62].

masses [62]. The solid horizontal line marks  $2\pi$  while the lower horizontal dot-dashed line represents the lattice free limit corrected [62] for the lattice time extent  $N_t$ . From Fig. 18 it is evident that for the  $\pi$  at  $T > T_c$ , the spatial or screening mass defect  $\Delta = 2\pi T - M(T)$  is decreasing more rapidly above  $T_c$  in the rank-1 separable model than is evident from the lattice simulations. This is consistent with the exponential behavior of the employed form factors. It is also consistent with the absence of quark vector self-energy amplitudes  $A(p_n) - 1$  and  $C(p_n) - 1$  through which interactions can be quite persistent in the asymptotic region. This can be demonstrated within the chiral limit ID model where those amplitudes are strong and indeed have the power law fall-off. As seen in Fig. 18, the resulting mass defect for both  $\pi$  and  $\rho$  is in fact too strong when compared with the lattice QCD simulations. This persistent self-interaction well above  $T_c$ , which slows the approach to free behavior such as Stefan–Boltzmann thermodynamics [48], may well be what is signaled by the lattice QCD data in Fig. 18.

## 7. Summary

Within a Poincaré-covariant approach to modeling QCD based on the DSE framework, the description of the ground state pseudoscalar and vector mesons has been reviewed at both zero temperature and finite temperature. The only approximation made is a self-consistent truncation of the set of DSEs, which respects the relevant vector and axial-vector WTI. In particular we choose the truncation wherein the employed quark propagators, the meson BSAs, and the quark-photon vertex are solutions of their DSEs in rainbow-ladder approximation. The two parameters are fixed previously by fitting the chiral condensate,  $m_{\pi/K}$  and  $f_\pi$ . We include all relevant Dirac amplitudes for the BSAs and their full dependence upon the angular variable  $k \cdot P$ .

The obtained pion and kaon electromagnetic form factors are in good agreement with the available data over the entire  $Q^2$  range considered, and the calculated charge radii are within the bounds

of the experimental values. The electromagnetic current is explicitly conserved in this approach, and there is no fine-tuning needed to obtain  $F_\pi(0) = 1 = F_{K^+}(0)$  and  $F_{K^0}(0) = 0$ . We also demonstrate explicitly that our results are (within numerical accuracy) independent of the momentum partitioning of the BSAs. The timelike behavior of the charge form factors exhibits the vector meson production resonances and this allows the associated vector meson strong decay constants to be extracted. The confining property of the quark self-energy dynamically produced in this work prevents the appearance of spurious  $\bar{q}q$  production effects. We also discuss transition form factors for the processes  $\gamma^* \rho \rightarrow \pi$  and  $\gamma^* \pi \rightarrow \gamma$  as well as the coupling constants for the associated physical radiative decay of the  $\rho$  and the electromagnetic decay of  $\pi^0$  as dominated by the axial anomaly.

We discuss the finite temperature extension of the approach as implemented by the Matsubara method. Both the chiral restoration and the deconfinement transitions are identified and a study of the critical exponents for the chiral transition is reviewed. Several versions of the model are employed to gain complementary viewpoints on the spatial  $\bar{q}q$  correlative modes with (pseudo)-scalar and vector meson quantum numbers. The corresponding masses  $M_\pi(T)$ ,  $M_\rho^T(T)$  and  $M_\rho^L(T)$  are found to be almost  $T$ -independent below  $T_c$  followed by a strong increase. This behavior is characteristic of lattice QCD simulations [60,62] and DSE studies [14,15,49]. The scalar mass  $M_\sigma(T)$ , an idealized chiral partner of the pion, decreases with  $T$  until it becomes equal to the pion mass at  $T_c$ ; above the critical temperature for chiral symmetry restoration the scalar and pseudoscalar modes are degenerate. Once the scalar mass drops below twice the pion mass, the decay width associated with the decay  $\sigma \rightarrow \pi\pi$  drops to zero, because of phase-space blocking [14,63]. Also the strong decay  $\rho \rightarrow \pi\pi$  decreases with temperature, and drops to zero at about 25 MeV above  $T_c$  due a phase-space blocking effect.

One should keep in mind that the results presented here follow from the response of the quark gluon content of the mesons to the heat bath. A

different phenomenon is the coupling of the meson modes to the many-hadron environment which introduces collisional broadening [61]. In order to study this effect, one has to go beyond rainbow-ladder truncation, and incorporate meson loop corrections. Also at zero temperature such corrections need to be studied in more detail: pion and kaon loops give rise to a nonzero width for the vector mesons. This would also allow for more realistic calculations of electromagnetic form factors in the timelike region, near and beyond the vector meson resonances. However, it is unclear how to add such corrections while preserving all relevant Ward identities.

**Acknowledgments.** We acknowledge useful conversations and correspondence with D. Blaschke, C.D. Roberts, and D. Jarecke. This work was funded by the National Science Foundation under Grant Nos. INT-9603385, PHY-9722429 and PHY-0071361 and by the Department of Energy under Grant Nos. DE-FG02-96ER40947 and DE-FG02-97ER41048; it benefited from the resources of the National Energy Research Scientific Computing Center, and the Ohio Supercomputer Center. Both authors are grateful for the hospitality of the University of Rostock where part of this work was conducted during several visits and also for the support of the Erwin Schrodinger Institute for Mathematical Physics, Vienna that made a visit possible and enjoyable.

## References

- [1] see e.g. H. J. Munczek and D. W. McKay, Phys. Rev. D **39**, 888 (1989) [Erratum-ibid. D **46**, 5209 (1989)]; D. Atkinson, H. de Groot and P. W. Johnson, Phys. Rev. D **43**, 218 (1991); H. J. Munczek and P. Jain, Phys. Rev. D **46**, 438 (1992).
- [2] M. R. Frank and C. D. Roberts, Phys. Rev. C **53**, 390 (1996) [hep-ph/9508225].
- [3] P. Maris and C. D. Roberts, Phys. Rev. C **56**, 3369 (1997) [nucl-th/9708029].
- [4] P. C. Tandy, Prog. Part. Nucl. Phys. **39**, 117 (1997) [nucl-th/9705018] and references therein.
- [5] C. D. Roberts and S. M. Schmidt, Prog. Part. Nucl. Phys. **45S1**, 1 (2000) [nucl-th/0005064].
- [6] R. Alkofer and L. von Smekal, Phys. Rep. in press (2001) [hep-ph/0007355].
- [7] C. J. Burden, C. D. Roberts and A. G. Williams, Phys. Lett. B **285**, 347 (1992); G. Krein, C. D. Roberts and A. G. Williams, Int. J. Mod. Phys. A **7**, 5607 (1992); P. Maris, Phys. Rev. D **52**, 6087 (1995) [hep-ph/9508323].
- [8] see e.g. K. Higashijima, Phys. Rev. D **29**, 1228 (1984); V. A. Miransky, Phys. Lett. B **165**, 401 (1985); D. Atkinson and P. W. Johnson, Phys. Rev. D **37**, 2290 and 2296 (1988); C. D. Roberts and B. H. McKellar, Phys. Rev. D **41**, 672 (1990).
- [9] P. Maris, C. D. Roberts and P. C. Tandy, Phys. Lett. B **420**, 267 (1998) [nucl-th/9707003].
- [10] P. Maris and P. C. Tandy, Phys. Rev. C **61**, 045202 (2000) [nucl-th/9910033].
- [11] P. Maris and P. C. Tandy, Phys. Rev. C **62**, 055204 (2000) [nucl-th/0005015].
- [12] P. Maris and P. C. Tandy, Phys. Rev. C **60**, 055214 (1999) [nucl-th/9905056].
- [13] A. Holl, P. Maris and C. D. Roberts, Phys. Rev. C **59**, 1751 (1999) [nucl-th/9808076].
- [14] P. Maris, C. D. Roberts, S. M. Schmidt and P. C. Tandy, Phys. Rev. C **63**, 025202 (2001) [nucl-th/0001064].
- [15] D. Blaschke, G. Burau, Y. L. Kalinovsky, P. Maris and P. C. Tandy, Int. J. Mod. Phys. A **16**, 2267 (2001) [nucl-th/0002024].
- [16] F. T. Hawes, P. Maris and C. D. Roberts, Phys. Lett. B **440**, 353 (1998) [nucl-th/9807056].
- [17] J. I. Skullerud and A. G. Williams, Phys. Rev. D **63**, 054508 (2001) [hep-lat/007028]; J. I. Skullerud, D. B. Leinweber and A. G. Williams, hep-lat/0102013.
- [18] P. Maris, to appear in the Proc. of the IV<sup>th</sup> Int. Conf. on **Quark Confinement and the Hadron Spectrum**, Vienna, Austria, July 2000, nucl-th/0009064.
- [19] P. C. Tandy, to appear in the Proc. of the Workshop on **Lepton Scattering, Hadrons and QCD**, Adelaide, Australia, March 2001, (World Scientific, Singapore), nucl-th/0106031.
- [20] D. B. Leinweber, Annals Phys. **254**, 328 (1997) [nucl-th/9510051].
- [21] C. Caso *et al.* [Particle Data Group Collaboration], Eur. Phys. J. C **3**, 1 (1998).

- [22] C. D. Roberts, these proceedings, nucl-th/0007054.
- [23] A. Bender, C. D. Roberts and L. Von Smekal, Phys. Lett. B **380**, 7 (1996) [nucl-th/9602012].
- [24] C. D. Roberts, Nucl. Phys. A **605**, 475 (1996) [hep-ph/9408233].
- [25] R. Alkofer, A. Bender and C. D. Roberts, Int. J. Mod. Phys. A **10**, 3319 (1995) [hep-ph/9312243].
- [26] C. J. Bebek *et al.*, Phys. Rev. D **13**, 25 (1976).
- [27] L. M. Barkov *et al.*, Nucl. Phys. B **256**, 365 (1985).
- [28] S. R. Amendolia *et al.* [NA7 Collaboration], Nucl. Phys. B **277**, 168 (1986).
- [29] J. S. Ball and T. Chiu, Phys. Rev. D **22**, 2542 (1980).
- [30] J. Volmer *et al.* [The Jefferson Lab F( $\pi$ ) Collaboration], Phys. Rev. Lett. **86**, 1713 (2001).
- [31] E. B. Dally *et al.*, Phys. Rev. Lett. **45**, 232 (1980).
- [32] S. R. Amendolia *et al.*, Phys. Lett. B **178**, 435 (1986).
- [33] JLab experiment E93-018, spokesperson O.K. Baker.
- [34] W. R. Molzon *et al.*, Phys. Rev. Lett. **41**, 1213 (1978) [Erratum-ibid. **41**, 1523 (1978)].
- [35] C. J. Burden, C. D. Roberts and M. J. Thomson, Phys. Lett. B **371**, 163 (1996) [nucl-th/9511012].
- [36] P. Maris and C. D. Roberts, Phys. Rev. C **58**, 3659 (1998) [nucl-th/9804062].
- [37] P. C. Tandy, Fizika B **8**, 295 (1999) [hep-ph/9902459].
- [38] P. Maris, Nucl. Phys. Proc. Suppl. **90**, 127 (2000), [nucl-th/0008048].
- [39] P. Maris and P. C. Tandy, in preparation, 2001.
- [40] H. J. Behrend *et al.* [CELLO Collaboration], Z. Phys. C **49**, 401 (1991); J. Gronberg *et al.* [CLEO Collaboration], Phys. Rev. **D57**, 33 (1998) [hep-ex/9707031].
- [41] G. P. Lepage and S. J. Brodsky, Phys. Rev. D **22**, 2157 (1980).
- [42] J. W. Van Orden, N. Devine and F. Gross, Phys. Rev. Lett. **75**, 4369 (1995).
- [43] K.L. Mitchell, PhD Thesis, Kent State University, unpublished (1995); P. C. Tandy, Prog. Part. Nucl. Phys. **36**, 97 (1996) [nucl-th/9605029].
- [44] H. J. Munczek and A. M. Nemirovsky, Phys. Rev. D **28**, 181 (1983).
- [45] N. Brown and M. R. Pennington, Phys. Rev. D **39**, 2723 (1989).
- [46] R. D. Pisarski and F. Wilczek, Phys. Rev. D **29**, 338 (1984).
- [47] G. A. Baker, B. G. Nickel and D. I. Meiron, Phys. Rev. B **17**, 1365 (1978).
- [48] D. Blaschke, C. D. Roberts and S. M. Schmidt, Phys. Lett. B **425**, 232 (1998) [nucl-th/9706070].
- [49] P. Maris, C. D. Roberts and S. M. Schmidt, Phys. Rev. C **57**, 2821 (1998) [nucl-th/9801059].
- [50] D. Blaschke, A. Holl, C. D. Roberts and S. M. Schmidt, Phys. Rev. C **58**, 1758 (1998) [nucl-th/9803030].
- [51] N. P. Landsman and Ch. G. van Weert, Phys. Rep. **145**, 141 (1987).
- [52] W. Florkowski and B. L. Friman, Acta Phys. Polon. B **25**, 49 (1994).
- [53] M. R. Pennington, hep-ph/0001183.
- [54] R. D. Pisarski, T. L. Trueman and M. H. Tytgat, Phys. Rev. D **56**, 7077 (1997) [hep-ph/9702362].
- [55] P. de Forcrand *et al.* [QCD-TARO Collaboration], hep-lat/9901017.
- [56] D. Blaschke, Yu. L. Kalinovsky and P. Tandy, in the Proc. of the XI Int. Conf. on **Problems of Quantum Field Theory**, Dubna, July 1998, 454 (1998) [hep-ph/9811476]; D. Blaschke and P. C. Tandy, in the Proc. of the ECT\* Int. Workshop on **Understanding Deconfinement in QCD**, Eds. D. Blaschke, F. Karsch and C. D. Roberts, (World Scientific, Singapore), 218 (2000) [nucl-th/9905067].
- [57] H. Ito, W. Buck and F. Gross, Phys. Rev. C **43**, 2483 (1991); Phys. Rev. C **45**, 1918 (1992); M. Buballa and S. Krewald, Phys. Lett. B **294**, 19 (1992); R. S. Plant and M. C. Birse, Nucl. Phys. A **628**, 607 (1998) [hep-ph/9705372].
- [58] C. J. Burden, L. Qian, C. D. Roberts, P. C. Tandy and M. J. Thomson, Phys. Rev. C **55**, 2649 (1997) [nucl-th/9605027].
- [59] A. Bender, D. Blaschke, Y. Kalinovsky and C. D. Roberts, Phys. Rev. Lett. **77**, 3724 (1996) [nucl-th/9606006].
- [60] F. Karsch and E. Laermann, Rept. Prog. Phys. **56**, 1347 (1993) [hep-lat/9304010].

- [61] R. Rapp and J. Wambach, Adv. Nucl. Phys. **25**, 1 (2000) [hep-ph/9909229]; R. Rapp and C. Gale, Phys. Rev. C **60**, 024903 (1999) [hep-ph/9902268].
- [62] K. D. Born *et al.* [MT(c) Collaboration], Phys. Rev. Lett. **67**, 302 (1991); A. Gocksch, Phys. Rev. Lett. **67**, 1701 (1991).
- [63] T. Hatsuda and T. Kunihiro, Phys. Lett. B **185**, 304 (1987); H. A. Weldon, Phys. Lett. B **274**, 133 (1992); D. Blaschke, Yu. L. Kalinovsky, S. Schmidt and H.-J. Schulze, Phys. Rev. C **57**, 438 (1998) [nucl-th/9709058]; M. K. Volkov, E. A. Kuraev, D. Blaschke, G. Röpke and S. Schmidt, Phys. Lett. B **424**, 235 (1998) [hep-ph/9706350].